Nonlinear effects of multifrequency hydrodynamic instabilities on ablatively accelerated thin shells

C. P. Verdon, R. L. McCrory
Laboratory for Laser Energetics, College of Engineering and Applied Science, University of Rochester, Rochester, New York 14623

R. L. Morse
Department of Nuclear Engineering, University of Arizona, Tucson, Arizona 85721

G. R. Baker,[a] D. I. Meiron, and S. A. Orszag
Department of Mathematics, Massachusetts Institute of Technology, Cambridge, Massachusetts 02139

(Received 24 August 1981; accepted 20 May 1982)

Two-dimensional numerical simulations of ablatively accelerated thin-shell fusion targets, susceptible to rupture and failure by Rayleigh–Taylor instability, are presented. The results show that nonlinear effects of Rayleigh–Taylor instability are manifested in the dynamics of the "bubble" (head of the nonlinear fluid perturbation) rather than in the dynamics of the spike (tail of the perturbation). The role of multiwavelength perturbations on the shell is clarified, and rules are presented to predict the dominant nonlinear mode-mode interactions which limit shell performance. It is also shown that the essential dynamics of strongly driven flows are governed by the classical Rayleigh–Taylor instability of an ideal, incompressible, thin fluid layer.

I. INTRODUCTION

Simulations of the hydrodynamic stability of ablatively accelerated thin-shell fusion targets have been the subject of a number of studies. The potential advantages of employing thin-shell targets to reduce the peak laser driving power required for a given performance have been demonstrated by a variety of published spherically symmetric hydrodynamic calculations.[1,2] The principle concern clouding the predicted performance of these targets is their hydrodynamic stability properties. The degradation of target performance of these types of designs is due to the ablative acceleration process itself which, from the continuous acceleration of the inwardly moving high-density shell by the low-density exhaust, gives rise to an unstable hydrodynamic configuration of the same generic form as the classical Rayleigh–Taylor interfacial instability of superposed fluids of different densities.[3,4]

Only recently have systematic treatments of the linear theory of unstable growth been used to determine the combined effects of compressibility, heat flow, and convection associated with the ablation process.[1,5–7] These analyses, when compared with classical analytic estimates, have indicated a substantial reduction in the linear growth rates for the potentially troublesome short wavelength modes. Nevertheless, even the reduced ablative growth rates so calculated are still sufficiently large that shell failure is predicted by extrapolation of the linear theory for reasonable target surface finish constraints.

Recent simulations of ablatively accelerated thin shells by lasers have indicated that the nonlinear evolution of unstable pure modes exhibits a spike amplitude saturation due to ablative mass removal.[8,9] The observed saturation demonstrated a departure from exponential growth, but the nonlinear mode evolution was seen to persist. The mode evolution for a finite-thickness shell approaches a limit because of fluid depletion of the shell material, in contrast to the classical case of a semi-infinite fluid layer. For the latter case, the nonlinear mode evolution shows a nearly constant "bubble rise" (velocity of the head of the nonlinear disturbance) at moderate times as the tip of the spike (disturbance tail) tends toward "free-fall." For a shell of finite thickness, a constant bubble rise velocity is prohibited by the finite mass reservoir of a fluid layer.

These earlier nonlinear calculations show other additional and important departures from classical nonlinear evolution. In particular, for the laser and target parameters considered, the observed flow near the ablation surface does not exhibit Kelvin–Helmholtz "roll-up" instability. Secondly, the unstable nonlinear modes exhibit a laminar structure, in the sense that density contours exhibit a smooth time-independent ordering near the ablation surface. Finally, it was observed in Ref. 8 that the longer wavelength modes (modes whose wavelength is greater than the most unstable wavelength of the linear growth rate curve, see Sec. II) are the most globally disruptive to the shell during the nonlinear phase of unstable growth. In obtaining the results reported in Ref. 8, the laser and target parameters were based on the results of a quasistationary model of ablation.[5,7,10]

An important addition to the results for the nonlinear evolution of the single frequency modes is the observation of a finite amplitude effect which was not reported in Ref. 8. The analysis of the Rayleigh–Taylor instability of a finite thickness shell shows that the transition from exponential growth to nonlinear mode evolution depends on the initial amplitude of the perturbation. This effect, due to the finite shell thickness, which is time dependent because of the ablation process, shows that the nonlinear modes, which determine an effective lifetime of the shell (see Sec. II) can be limited by proper attention to the target surface finish.

[a] Present address: Department of Mathematics, University of Arizona, Tucson, Arizona 85721.

 0031-9171/82/091653-22$01.90

One of the principal objectives of the present paper is to extend our previous results by following the nonlinear evolution of a combination of unstable modes. We show that the effective shell lifetime may be decreased substantially by nonlinear mode-mode interactions, but that the laminar nature of the unstable structure exhibited for pure modes is still observed. These multifrequency results allow one to obtain surface finish requirements which will be required for successful shell implosions. In this paper we also indicate that results obtained for an incompressible, inviscid, finite fluid layer lead to a synergistic understanding of both the single- and multifrequency nonlinear results obtained in the full ablative numerical simulations. The ideal fluid results for the nonlinear modes are obtained using new, computationally efficient, boundary-integral techniques.[11,12] These techniques allow a rather exhaustive study of nonlinear mode-mode effects which would be prohibitive to analyze using full laser fusion implosion two-dimensional simulations. Additionally, the boundary integral techniques are extensible to three dimensions where little, if any, research results are presently available. In the text we present these new results for the large amplitude behavior of unstable Rayleigh–Taylor modes of an incompressible, inviscid, finite mass fluid layer whose Atwood number (α) is unity on the bounding surfaces. We indicate how the ideal fluid results, together with unperturbed ablatively accelerated shell calculations, can be used to give quantitative estimates of the onset of hydrodynamic failure due to the multifrequency Rayleigh–Taylor instability of ablatively accelerated shells.

Section II of this paper deals with a single wavelength Rayleigh–Taylor mode and the observed finite amplitude effects. In Sec. III, we introduce the nonlinear results obtained for an ideal inviscid incompressible fluid using boundary integral techniques.[11] Section IV treats the two-frequency mode simulations using the full two-dimensional simulation code and compares the results with multifrequency results for an ideal fluid. Based on this comparison, we use the boundary integral code calculations to obtain estimates for the most disruptive nonlinear mode-coupling effects expected to be important in ablatively accelerated thin shells. Section V summarizes our results.

II. NONLINEAR EVOLUTION OF THE SINGLE-FREQUENCY RAYLEIGH–TAYLOR INSTABILITY

In this section we review our previously reported results and extend these results to describe the nonlinear evolution of the single frequency Rayleigh–Taylor instability for ablatively accelerated thin shells. The full two-dimensional simulations were carried out using the initialization procedure described in Ref. 8: A planar slab of fully ionized material (carbon, $Z = 6$) is accelerated between two rigid, parallel slip surfaces by ablation pressure. The ablation is driven by a constant absorbed laser irradiance deposited at a critical density of $n_e = 10^{21}$ cm^{-3}. The simulations are begun with an initially uniform shell density (2 g/cm^3) and thickness (3 μm), and run with a one-dimensional code until a quasi-steady ablative flow is established near the shell surface. Dimensionless, rather than physical values, could have been used in presenting the two-dimensional results, but it was felt that representative physical values make it easier for the reader to identify cases of practical interest for laser-driven ablation. At the time t_i, the simulation is made two-dimensional, a perturbation that is localized near the ablation surface is applied, and the time evolution of the flow is then followed using the two-dimensional Lagrangian computer code, DAISY.

A summary of the calculational procedure used in DAISY is given in Appendix A. In Appendix A, we also summarize the results of test calculations used to illustrate the accuracy of our computational procedures. In the DAISY simulations, the computational region extends in y a distance equal to one-half the wavelength and the diagrams are constructed by periodic replication in the y direction.

A. Flow initialization

The perturbation we apply is a displacement of the grid locations of mass points in the slab. We choose the applied perturbation ξ to be incompressible (so that the target density and mass is held constant) by choosing the form

$$\xi = \nabla \times \mathbf{B}, \tag{1}$$

where $\mathbf{B}$ is a vector potential. The simulations were carried out in planar geometry where the unperturbed target surfaces correspond to the surfaces $x = \text{const}$. The laser is incident from the right in the figures, and the acceleration is directed along the negative x axis. The perturbation is given by Eq. (1) with $\mathbf{B} = \hat{z}B_z$, where

$$B_z = (A/k_y)\sin(k_y y)\,\mathrm{sech}[k_y(x - x_m)]; \tag{2}$$

and x_m is the point of maximum shell density. The choice of a divergence-free perturbation ensures that we do not place the fluid in tension or compression, avoiding transients not of interest in the present study.

For $|k_y(x - x_m)| \gg 1$, the perturbation [Eqs. (1),(2)] has the form of the linear Rayleigh–Taylor mode[3,4] at a density discontinuity between two superposed fluids, and is a smooth function of x at smaller $|k_y(x - x_m)|$. Of the forms of B_z that we have used, with given values of $k_y A$, Eq. (2) causes the least transient disturbance immediately after initialization. For the ablative cases illustrated here, the slab will be consumed by ablative mass removal at a burn-through time, $t_b \simeq 140$ psec for the irradiance examples using $I = 10^{15}$ W/cm^2. The resolution that is required for accurate analysis was found to be on the order of 72 points per wavelength (λ_y) in y, and results in totals of roughly 9000 and 11 000 zones, respectively, for the single-frequency and two-frequency perturbations considered. The resulting resolution is similar to that reported in Lagrangian boundary integral simulations of large nonlinear amplitudes for the classical Rayleigh–Taylor instability of a semi-infinite layer of incompressible inviscid fluid in vacuum.[11]

Figure 1 shows the time history of the one-dimensional (unperturbed) calculation of the density and temperature profiles used in the present analysis. The intensity chosen was $I = 1 \times 10^{15}$ W/cm^2. A one-temperature description of thermal conduction is employed. In order to compare our results with the steady flow results of Ref. 7 we use a $\ln \Lambda \equiv 5$ in the Spitzer expression for the electron thermal conductivity.[13] When the restrictions of constant $\ln \Lambda$ and Z are re-

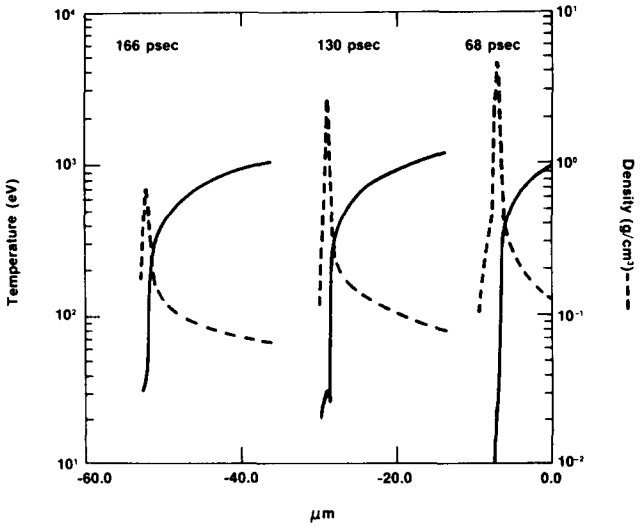

FIG. 1. Time sequence of temperature and density profiles for the one-dimensional simulations of the laser-driven ablation of a 3 μm fully ionized carbon slab in planar geometry. The laser is incident from the right, and the irradiance at the critical surface is 10^{15} W/cm^2. Note that by 166 psec, the laser burns through the slab, as indicated by the drop in the peak of the density profile.

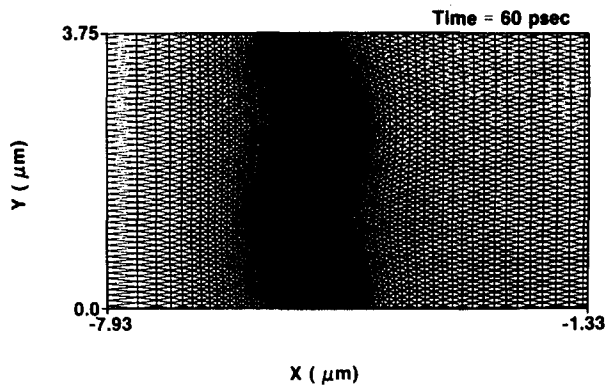

FIG. 2. Mesh plot illustrating the two-dimensional DAISY grid at the time a perturbation is initialized (60 psec) at the ablation surface. The figure illustrates a distortion of wavelength 2.5 μm with an amplitude-to-wavelength value $A/\lambda_y = 0.1$.

moved, the effective irradiance required to achieve the same fractional ablative mass removal is of the order of a few times 10^{14} W/cm^2.

Corresponding to these irradiances (10^{14} W/cm^2) for 1.05 μm light, the effect of suprathermal electrons is small[14] and is not included in our simulations. Since our principal interest is the unstable behavior of ablatively accelerated targets, particularly those driven by lasers of wavelengths 1 μm or less where the absorbed irradiances of interest are of order 10^{14} W/cm^2 for 1.05 μm light or of order 10^{15} W/cm^2 for 0.35 μm light, neglect of these suprathermals is justified. Furthermore, we have used an uninhibited thermal electron transport model. Because we are interested in moderate irradiances and the behavior of instabilities near the ablation surface, i.e., far from the critical surface, inhibited transport models would have little or no effect on our results.[15]

Figure 2 illustrates the initial grid used in the DAISY simulations. It can be seen that the density of zones is quite high in the region near the shell (appearing as a solid black region in the figure at the time of initialization).

In Fig. 2, and all other DAISY plots in this paper, we note that the critical surface, where absorption of the laser energy occurs, is far to the right of the plotted region (corresponding to a density of approximately 3×10^{-3} g/cm^3). This is a consequence of the quasistationary profile established for the choices of irradiances used in our examples. The interested reader is referred to Refs. 5 or 15 for additional details describing these solutions. Figure 3, adapted from Ref. 5, illustrates the linear growth rates as a function of wavenumber obtained from the two-dimensional code (DAISY) together with the stationary ablative flow perturbation results of Ref. 7. In the results plotted in Fig. 3, the two-dimensional calculations were initialized with an amplitude-to-wavelength ratio $A/\lambda_y = 0.001$ in order to ensure that linear effects would result. In Appendix A, we illustrate the agreement between small amplitude DAISY calculations and analytic results for several test cases. It can be seen that both the DAISY results and the steady flow results show growth rates γ lower than those given by the classical theory $\{\gamma_{cl} = \int_0^t [ka(t)]^{1/2}dt/t\}$, where $a(t)$ is the time-dependent acceleration calculated at the ablation surface. From Fig. 3 it can be seen that the DAISY results for the linear growth rates lie between $27 < \tilde{\rho}_p < 50$, where $\tilde{\rho}_p$ is a single parameter characterizing the stationary solutions of Ref. 5. This parameter is defined as the ratio of maximum density in the shell to the isothermal sonic point density and is a function of I, Z, ρ, etc. At the time of initialization the value of $\tilde{\rho}_p$ from the unperturbed simulation is approximately 35. Steady flow results have shown that $\tilde{\rho}_p$ is a sensitive function of target conditions, irradiance, etc.; indeed the growth rates of the stationary flow models compare quite closely wiht the present time-dependent DAISY results.

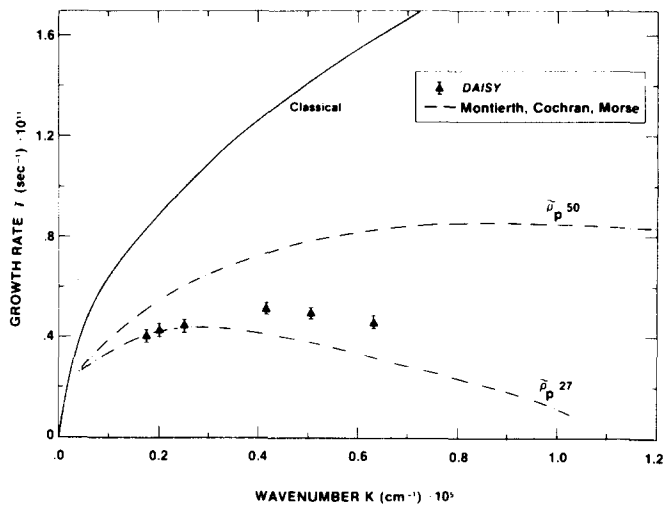

FIG. 3. Linear growth rate spectrum, $\gamma(k)$, generated by DAISY simulations of small initial amplitude-to-wavelength perturbation ($A/\lambda_y = 0.001$) on the carbon slab irradiated at 10^{15} W/cm^2. The dashed curves represent perturbation calculations obtained in Ref. 7 from the stationary flow model of ablation for two different values of the ratio of the density at the ablation surface to the density at the isothermal sonic point ($\tilde{\rho}_p$). The "classical" growth rate γ_{cl} is plotted for reference.

B. Perturbation results

The perturbation results obtained from the stationary model of ablation are in agreement with previously published time-dependent perturbation solutions.[1-6] In contrast to the case of an infinite fluid layer, for a finite thickness shell two quantities are required to determine the nature of the instability: A/λ_y and $A/\Delta x$, where Δx is the shell thickness. Both perturbation treatments indicate that the most dangerous single-frequency mode, as indicated by a local maximum is the linear growth rate spectrum, occurs for a wavenumber k ($\equiv 2\pi/\lambda_y$, where λ_y is the perturbation wavelength) for which the product $k\Delta x = O(1)$. The case, $I = 10^{15}$ W/cm^2 and $k = 2.5\times 10^4$ cm^{-1} ($\lambda_y = 2.5\,\mu$m) is seen from Fig. 3 to be near the maximum unstable linear growth rate in the $\gamma(k)$ curve, and was chosen here, together with the shorter wavelength case ($\lambda_y = 1.0\,\mu$m), to follow the nonlinear evolution of unstable modes.

It should be noted that a subset of the results for the cases reported here was previously discussed in Ref. 8. Our purpose in reviewing these data is to illustrate finite amplitude effects not previously reported and to give a direct comparison of the effect of different initial amplitudes in the fully developed nonlinear regime. Additionally, we summarize the results for several other wavelengths whose linear growth rates are near the maximum for comparative purposes.

In Fig. 4 we show the time evolution of the density contours for a 1.0 μm wavelength perturbation whose initial amplitude-to-wavelength ratio (A/λ_y) is 0.1. For this case, $k\Delta x > 1$ as measured by the rms distance separating contours of the initial material density (2 g/cm^3) at the time of initialization. It can be seen that the density contours which evolve in time deform into the usual bubble and spike form typical of the classical Rayleigh–Taylor instability.[11,16-19] It can also be seen that on both the anterior and posterior surfaces of the target there appears to be a laminar structure illustrated by the time-independent ordering of the density contours, and there is no evidence of a vortex sheet roll-up on the front surface which one might anticipate due to a Kelvin–Helmholtz-like instability.[11,17]

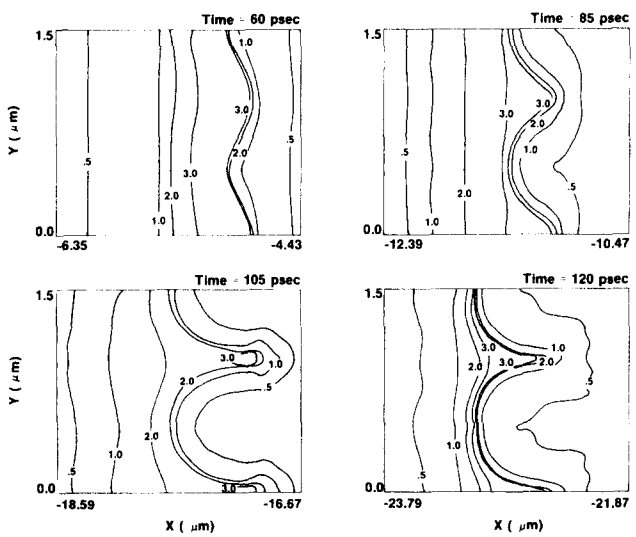

FIG. 4. Time evolution of the density contours (g/cm^3) for a $\lambda_y = 1.0\mu$m, ($A/\lambda_y = 0.1$) perturbation on the carbon slab irradiated at 10^{15} W/cm^2.

Figure 5 illustrates the evolution of the density and temperature contours together with the velocity vector (wind) plots relative to the center of mass for a 2.5 μm wavelength perturbation whose initial $A/\lambda_y = 0.1$ (see Fig. 2). For this case, $k\Delta x$ is of order unity; it can be seen that there are some qualitative and quantitative differences between the results of Figs. 4 and 5. The density contours indicate that there is still a laminar structure, but note the formation of a small reverse jet or anti-spike at the rear surface of the shell in Fig. 5. The cause of the anti-spike is due to the formation of a high-pressure region, which forms in the region behind the spike and causes material to be pushed backwards. It can also be seen that the bubble shown in Fig. 5 has a broader and flatter appearance than that illustrated for the Fig. 4 case.

In Fig. 5, the wind plots show that material near the spike tip is being convected rapidly towards the laser with no Kelvin–Helmholtz (K–H) instability leading to roll-up of spike material. For all the cases presented in this paper, roll-up was not observed. In order to minimize numerical errors, no remeshing (rezoning) was used in our computations. Reduced irradiances from the values considered here may result in significant K–H instability (see Sec. III) and, hence, significant roll-up of spike material. Without such roll-up, the Lagrangian DAISY code is quite robust and requires no remeshing. The close spacing of the temperature and density contours near the spike tip, in contrast with the wide spacing near the top of the bubble region indicates higher ablation near the spike. The results plotted in Fig. 5 also illustrate that the zoning resolution in the region of interest even at late times in the simulations is quite adequate to resolve the details of the spike and bubble structure of the unstable flow. In particular, from either the contour plots or the wind plots of Fig. 5, it is seen that thermal, velocity, and density scale lengths are resolved over many grid locations. Such resolution is required in order to ensure that numerical diffusion effects are not responsible for our observed results.

To illustrate the unstable growth of the perturbation, we plot the difference between the positions of the $\rho = 2$ g/cm^3 contours at the bubble center and spike tip as a function of time. These results are illustrated in Fig. 6 for the two unstable cases of Figs. 4 and 5. We note that if a different value of density, e.g., 1 g/cm^3 or 1.5 g/cm^3 instead of 2 g/cm^3, is chosen to measure either Δx or the amplitude of the unstable modes then the results for the growth rate obtained using the DAISY code change by no more than 5%. It is not reasonable to choose much lower-density values, because one then moves significantly away from the ablation surface. As a second check on our procedure, the alternative prescription of Ref. 5, where the unstable mode amplitude was measured using the rms value of the time evolution of Lagrangian markers, gave values in essentially exact agreement with the present procedure with a density of 2 g/cm^3. It can be seen that both examples exhibit the linear theoretical temporal behavior (cosh γt) early in time, followed by decreased growth resulting in an approximately quasistationary large-amplitude behavior. For the 1.0 μm perturbation note that ablation actually burns off the tip of the spike during the

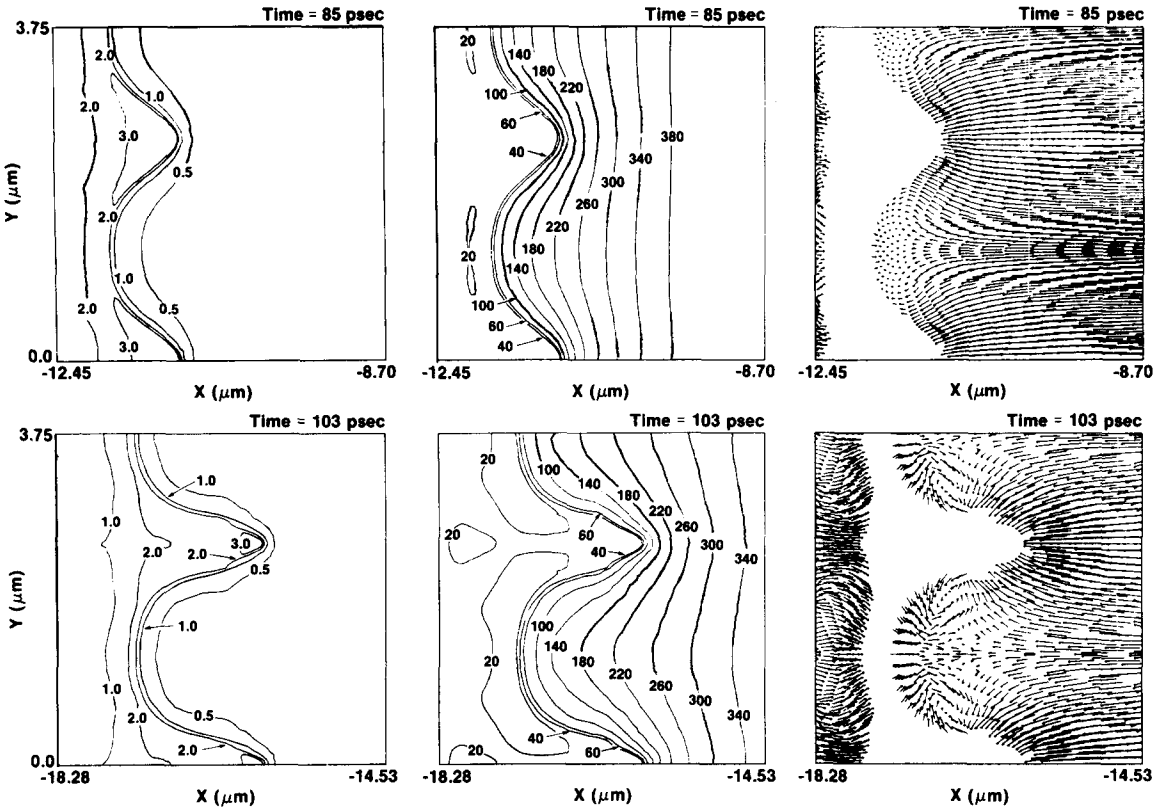

FIG. 5. Time evolution of density (g/cm^3), temperature (eV) and velocity flow field for a $\lambda_y = 2.5\,\mu m$, $A/\lambda_y = 0.1$ perturbation on the carbon slab irradiated at 10^{15} W/cm^2. Velocity vectors are shown only for those zones whose density is less than 1.0 g/cm^3.

simulation as evidenced by the decrease in the spike-to-bubble amplitude late in time. This overshoot feature has been observed in a number of simulations.

It is important to note that the finite spike amplitude seen in Fig. 6 does not indicate a mode saturation: A plot of the shell thickness as a function of time, as measured by the distance between the front and back surface $\rho = 2$ g/cm^3 contours at the thinnest position (at the bubble center), shows that the mode is still evolving.

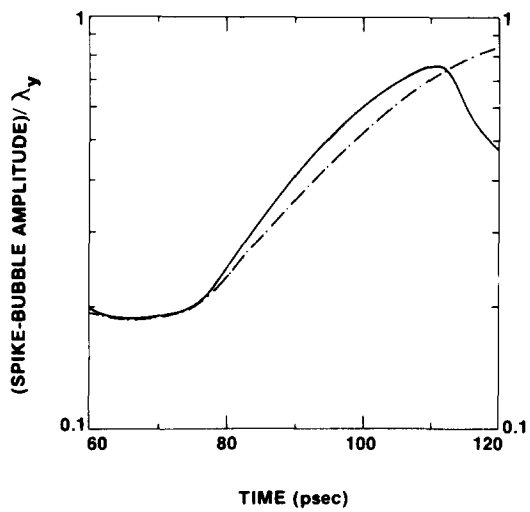

FIG. 6. Spike amplitude time history of the surface distortion (defined as the separation distance between the center of the bubble and tip of the spike as measured by the $\rho = 2$ g/cm^3 contours) for both the 2.5 μm (dashed curve) and 1.0 μm (solid curve) perturbations (see Figs. 4 and 5).

An examination of the fluid velocity profiles shows that as the mode evolves, material is continually being swept out of the shell. This convective mass motion causes the shell to thin continually in time. Figure 7 illustrates this effect graphically: The unperturbed shell thickness as a function of time is compared with the thickness at the bubble center for the 1.0 μm and the 2.5 μm perturbed cases. The shell thinning rate in the 1.0 μm case is less than that of the longer wavelength case, but both thinning rates are significantly greater than that due to ablation alone.

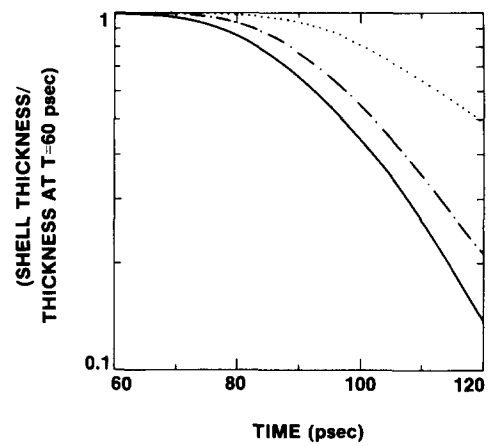

FIG. 7. Shell thickness, measured in units of the shell thickness at t_i at the bubble center (thickness as determined in Fig. 6) for both the 1.0 μm perturbation (see Fig. 4), shown by the dashed curve, and the 2.5 μm perturbation (see Fig. 5) shown as a solid line. For reference, the shell thickness of the unperturbed case is shown (dotted line) to illustrate the time dependence of shell thickness due to ablation alone.

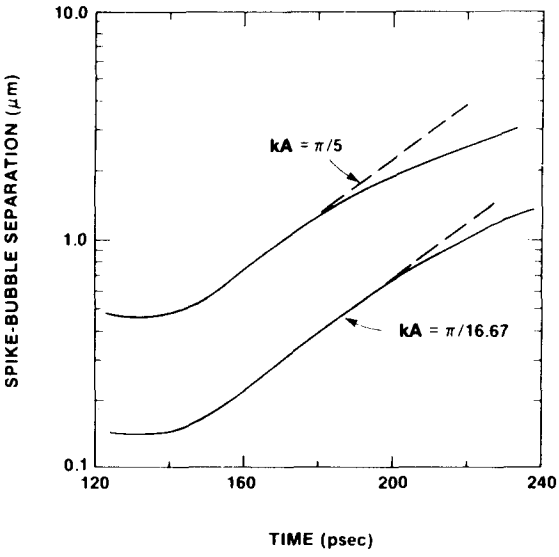

FIG. 8. Spike amplitude, defined as in Fig. 6, as a function of time for two different initial amplitude-to-wavelength ratios [$A/\lambda_y = 0.1$ (kA = $\pi/5$) and $A/\lambda_y = 0.03$ (kA = $\pi/16.67$)] for a 2.5 μm perturbation. The absorbed laser irradiance for this case is 3×10^{14} W/cm^2 and the carbon slab is not consumed by ablative mass removal until approximately 250 psec. Note that the initial amplitude of the mode determines the amplitude at which departure from linear growth (dashed lines) occurs.

An important feature of the simulations is a nonlinear effect due to finite shell thickness. For $I = 3\times10^{14}$ W/cm^2, the amplitude of the unstable mode defined as before as the separation between the tip of the spike and center of the bubble, is plotted as a function of time in Fig. 8. Figure 8 shows that for the 2.5 μm case, with $A/\lambda_y = 0.1$ (kA = $\pi/5$) initially, the departure from linearly unstable growth occurs at an amplitude of approximately 1.5 μm, in contrast to the case with $A/\lambda_y = 0.03$ (kA = $\pi/16.67$), where it occurs at an amplitude of approximately 0.8 μm. This same phenomenon has been seen over a range of laser irradiances: Figure 9 illustrates the behavior for a higher irradiance (10^{15} W/cm^2) with the same wavelength ($\lambda_y = 2.5\,\mu$m).

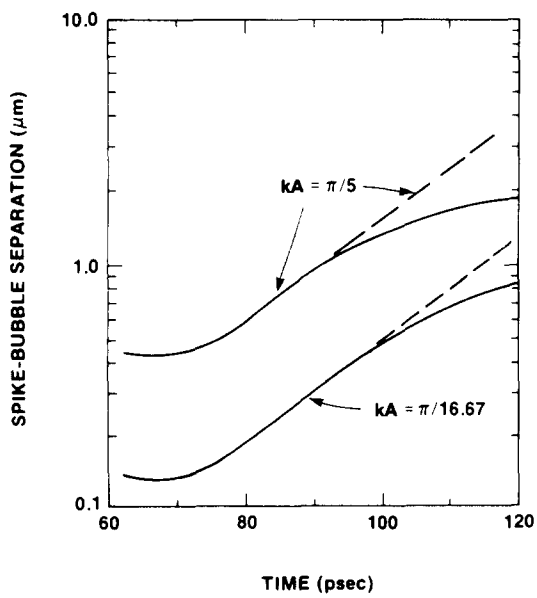

FIG. 9. Spike amplitude as a function of time for a 2.5 μm perturbation with different initial amplitude-to-wavelength ratios (see Fig. 8). The absorbed laser irradiance is 10^{15} W/cm^2. The dashed curves indicate the spike amplitudes predicted using a linear growth rate.

C. Effective shell lifetime

The finite amplitude effect observed in Figs. 8 and 9 determines the effective lifetime of the shell. In determining the time scales of interest, it is useful to define a burn-through time for the shell, defined as $t_b = [(1/m)(dm/dt)]^{-1}$, where m is the shell mass. However, for this definition to be quantitatively meaningful, it is necessary to unambiguously define the effective time-dependent shell mass, m in the formula which is to be associated with the acceleration of material due to ablation. We define m to be the sum of the mass over all zones whose density exceeds half of the initial shell density. The quantity t_b is the dimensional time required to characterize ablative time scales. Since the simulations we are describing are in planar geometry, there is no implosion time, but in practice t_b can be thought of as being approximately equal to the implosion time.[5] This is a consequence of the stationary model of ablation, in analogy with a simple rocket model, maximum transfer of absorbed energy to the imploding shell is achieved when the ablated fraction of the shell at culmination is of the order of 80%.[5,15]

Although in our simulations the ablation rate is highest at the spike tip, ablation still proceeds along the entire front surface of the shell and ablative rupture occurs first at the thinnest portion of the shell. We identify the final failure mode as ablative rupture as opposed to hydrodynamic rupture, because at late times in the simulation the density at the thinnest portion of the shell drops as the temperature rises. This effect is analogous to the burn-through illustrated at late times in the one-dimensional calculation of Fig. 1. Furthermore, in the incompressible simulations discussed in Sec. III, the thickness of a finite fluid layer is decreasing no faster than exponentially in time, at least for intermediate times. Ablative rupture is enhanced by the instability because when the shell thickness at some position approaches a small fraction of its original thickness it tends to burn through there. Thus an effective measure of shell lifetime, which is shorter than t_b when perturbations are present, is the time required for shell material (whose density exceeds half of the initial shell density in accordance with our definition of m in the expression for t_b) to achieve a limiting thickness at the thinnest portion of the shell. A reasonable value of the limiting thickness is 20% of the initial shell thickness. The tacit assumption is that the irradiances chosen are sufficiently high so that additional shell thinning not included in the one-dimensional ablation calculations will result in shell burn-through for most designs. Alternatively, the simulations can be continued to burn through at the shell's thinnest positions, and in some cases this has been done. The choice of 20% of the initial thickness results in substantial computational savings and has been found to be satisfactory in carrying out the simulations reported here.

D. Center of mass motion of the shell

The simulations show the important result that both the center-of-mass motion and the acceleration of the shell

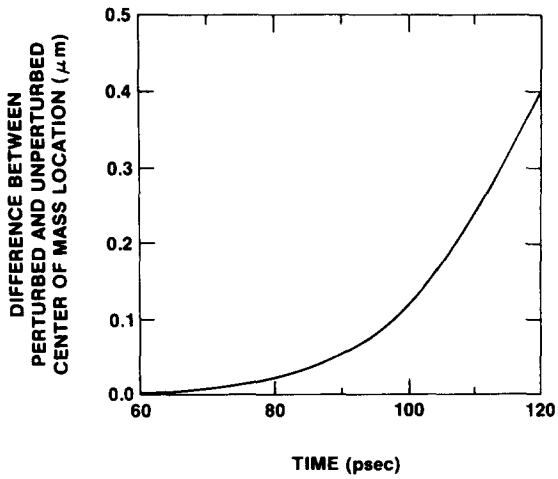

FIG. 10. Time history of the difference between the x center-of-mass location between the perturbed $\lambda_y = 2.5\,\mu$m, $A/\lambda_y = 0.1$ case and the unperturbed case.

are virtually unchanged by the presence of the unstable Rayleigh–Taylor mode until ablative rupture of the shell occurs. In Fig. 10 we plot the difference between the center-of-mass positions for an unperturbed calculation and a perturbed calculation ($A/\lambda_y = 0.1, \lambda_y = 2.5\,\mu$m) as a function of time. In Fig. 10, the center-of-mass of the shell is calculated from the average of all zones whose density exceeds half the original material density (i.e., 1.0 g/cm^3). For all the calculations presented in this paper, we have employed equal mass zoning, so the plotted displacement is also the mass weighted displacement. The center-of-mass for the unperturbed calculation moves more than 20 μm, while the difference plotted in Fig. 10 reaches a maximum of only 0.4 μm. For other perturbation calculations presented in this paper, this difference is even less than the case illustrated in Fig. 10. In the unperturbed case, the ablation rate is lower than that measured at the tip of the spike in the perturbed case. The ablation pressure at the tip of the spike is larger than that at the center of the bubble, due to the temperature differences in the ablated material nearest the target surface. The net effect

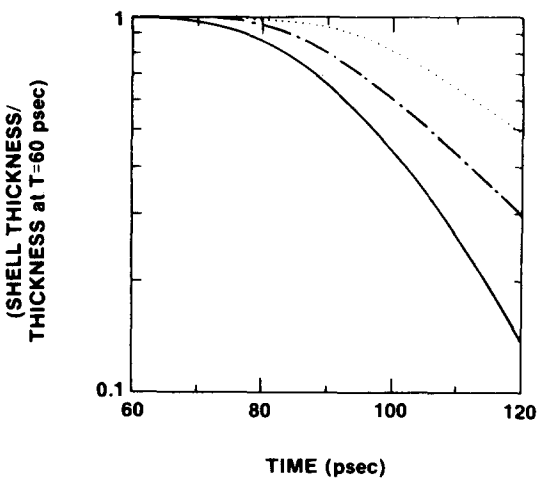

FIG. 11. Shell thickness, defined as in Fig. 7, as a function of time for the two different initial amplitudes (see Fig. 9) of a 2.5 μm perturbation. For the solid curve, $A/\lambda_y = 0.1$; for the dashed curve $A/\lambda_y = 0.03$. The dotted line illustrates the shell thickness for the unperturbed case.

of this behavior is the nearly constant saturation observed in the amplitude of spike-to-bubble distances in Figs. 8 and 9. Additionally, although the effective mass of the perturbed shell is less, the ablation process is less efficient in accelerating the center-of-mass of the system. The numerical results show that a correspondingly larger amount of energy is invested in fluid flow from the fluid region near the bubble into the spike interior, as opposed to motion normal to the target surface. As a consequence of this difference in kinetic energy partitioning, the center-of-mass motion of the perturbed and unperturbed cases is nearly constant (within 5% of each other for the simulations reported here) unless ablative rupture occurs. The nearly constant bubble rise velocity observed at moderate times allows one to estimate the effective lifetime of a perturbed shell by extrapolation to the 20% thickness time (see Figs. 7 and 11).

E. Safe aspect ratios

The structure of the density profiles observed in Figs. 4 and 5, as indicated by their laminar shape and time-independent ordering (as opposed to disordered or turbulently mixed profiles[20,21]) suggests that the upper limit of aspect ratios imposed by instability on these systems can be extended to higher values than previously deduced on the basis of extrapolation from linear theory. The predictions from linear theory limited initial aspect ratios to values of the order of five or less.[1,22–24]

In applying the results of simulations of planar slabs to spherical shells, it should be understood that planar geometry corresponds to the limit of large aspect ratio. As the aspect ratio decreases, the spherical divergence of the ablative flow, relative to the shell acceleration, becomes increasingly important in determining the character of the flow. Calculations with the stationary flow model of ablation indicate that for burn-through times resulting in good hydrodynamic efficiency, acceleration plays a dominant role and the planar approximation is valid, provided the inflight aspect ratio (defined below) is of the order of or greater than 30. According to Ref. 5, where the dimensionless parameter $\tilde{g}$ is effectively a measure of the importance of acceleration relative to divergence.

Although it is the initial aspect ratio of the target that is most often quoted in discussions of spherical target design and performance, it is the inflight aspect ratio of the shell that is of importance in determining the stability properties of the shell to Rayleigh–Taylor instability.[5] The inflight aspect ratio is defined by $r(t)/\Delta r(t)$, where $\Delta r(t)$ is the separation distance between two surfaces of equal density (the original shell material density) and $r(t)$ is the mean radial position of these surfaces.

To estimate the largest inflight aspect ratio which may be successfully employed, which we refer to as the safe aspect ratio Q, we use the present analysis of planar slabs (where shell thinning to 20% is employed as our definition of failure) to determine the distance the shell moves when it achieves this minimum safe thickness normalized by its thickness when the perturbation is initially applied. Using this definition of Q, shell motion over larger distances corresponds to burn through or rupture by ablation.

As an example of this procedure for estimating Q we consider the case where $I = 10^{15}$ W/cm^2 and the perturbation wavelength λ_y is 2.5 μm. From Fig. 7, it is seen that this mode is more dangerous for the same initial amplitude-to-wavelength ratio, than the shorter wavelength mode with $\lambda_y = 1.0$ μm. At the initialization time, the unperturbed shell thickness is of order 0.5 μm which results from compression and ablation of the original 3.0 μm shell. The simulation shows that the shell thickness at the bubble center is 0.1 μm at time 115 psec when the shell has moved 16.1 μm, so the safe aspect ratio Q is approximately 32. For the smaller initial amplitude perturbation, a reduction by approximately a factor of three in initial amplitude effectively increases the shell lifetime by about 20 psec and results in a safe aspect ratio of nearly 40. The longer effective lifetime of the shell is apparent by reference to Fig. 11, where we plot the shell thicknesses as a function of time for the unperturbed case and for the $A/\lambda_y = 0.10$ and $A/\lambda_y = 0.03$ perturbed cases. Relating the safe inflight aspect ratio to the more conventionally employed initial aspect ratio, the above Q's correspond to an initial aspect ratio of approximately ten. For example, this value of the initial aspect ratio is obtained by dividing 3 μm (the shell thickness at $t = 0$) into the 30 μm that the center-of-mass has moved before failure for the 2.5 μm wavelength ($A/\lambda_y = 0.03$) simulation. Thus the range of initial aspect ratios which may be used is extended from five, based on conjecture from linear theory,[1] to approximately twice that value.

F. Surface finish requirements

It may appear that the amplitude-to-wavelength ratios in the examples seem large compared with present fabrication capabilities. We point out that the initial ($t = 0$) target surface finish requirements are substantially more restrictive. Extrapolation from t_i to $t = 0$, using the linear growth rate (indicated by the slope of the dashed lines in Fig. 9) and accounting for the approximately 10 psec startup time (corresponding to the early time behavior of the cosh γt linear theory result) which occurs prior to exponential growth, results in an initial fabrication tolerance which is 20 times more restrictive than the A/λ_y ratio at t_i. This argument is only approximate. The initialization procedure employed to study the stability of the ablation surface in this paper neglects early time transient effects,[1,24] which may change the present estimates, but only by a factor of order two or so. Furthermore, nonlinear effects can be avoided by requiring the initial surface finish to be smoother, typically $A/\lambda_y \leqslant 0.1$ for $k\ (\equiv 2\pi/\lambda_y)$ over the entire range, $1/3 < k\Delta x < 3$.

In summary, two quantities are important in determining the unstable behavior of a finite fluid layer; (1) the amplitude-to-wavelength ratio of the mode (A/λ_y), which fixes both the growth rate and the penetration depth of the mode,[3,4] and (2) the amplitude-to-layer thickness ratio of the mode (for fixed A/λ_y, this is equivalent to specifying $k\Delta x$). The choice $A/\lambda_y < 0.1$ to avoid nonlinear initial behavior is based on the results of Fig. 3 by examining the linear growth rates (e.g., see Fig. 9) obtained by increasing the amplitude-to-wavelength ratio in DAISY simulations until the observed growth rates no longer agree with those of Fig. 3. This procedure unambiguously determines the range of validity of linear mode evolution, given the insensitivity of the growth rates to Δx discussed above. Reference to Fig. 3 shows that the linear growth rates over this range in k are nearly equal. On the basis of this observation, it may be argued that the initial surface finish required, based on the smallest wavelength of interest, reduces the initial tolerance by another factor of 3, resulting in initial A/λ_y values to avoid nonlinear effects of order 5×10^{-4} or less.

These estimates indicate that the surface fabrication requirements are sufficiently restrictive so that the nonlinear effects we are discussing are of importance in present and proposed inertial fusion implosion experiments.

G. Effects of irradiance and convergence

For the lower-irradiance case illustrated ($I = 3 \times 10^{14}$ W/cm^2), the ablation rate is sufficiently small that the burn-through time of the unperturbed system is greater than 250 psec. The effective aspect ratios which may be employed for this system are smaller; for the 2.5 μm perturbation whose initial amplitude-to-wavelength ratio A/λ_y is 0.1 ($kA \sim \pi/5$), $Q \sim 20$, and for the smaller initial amplitude case, $A/\lambda_y = 0.03$ ($kA \sim \pi/16.67$), $Q \sim 30$. These A/λ_y values at t_i are reduced by approximately the same factor (25 to 30) as in the higher-irradiance example when extrapolated from t_i back to $t = 0$. It is significant that the lower ablation rate is less effective in mitigating the unstable mode behavior. This result was inferred by extrapolation in Ref. 1 and more recently illustrated using both linear analysis and numerical simulation.[8,9] In Ref. 9 it was also demonstrated that the predominant smoothing mechanism is due to nonlinear thermal conduction and not to convective stabilization.[25] We concur with this conclusion. The velocity gradients near the ablation surface (e.g., see Fig. 5) are never large enough to overcome the destabilizing acceleration due to the pressure gradient in these examples. Although higher irradiances may effectively increase the aspect ratio which may be successfully employed, the irradiances required may result in a decreased hydrodynamic efficiency for the implosion. This results from the burn fraction of the shell being higher than that which is required to obtain maximum hydrodynamic efficiency.

Target performance may be degraded by the inability of a highly distorted shell to act as a pusher that efficiently delivers its kinetic energy to the fuel at the time of peak compression. The effects of converging geometry on the behavior of target implosion systems in the presence of the types of shell distortion seen here require further investigation. It is plausible that successful target reoptimization can be achieved by calculations which consider the combined effects of nonlinear shell distortion and convergence. Such calculations, however, require consideration of the nonlinear multifrequency effects which we discuss in Sec. IV.

H. Comparison with ideal fluid motion

The finite initial amplitude effect observed is principally due to the nonlinear mode evolution in a finite thickness fluid layer (see Sec. III). A linear analysis of the instability of

a liquid sheet of finite thickness, for the case of a liquid initially at rest, yields a growth rate independent of the shell thickness. Furthermore, linear analysis shows that the two free surfaces of a finite shell are effectively decoupled when $kh \gtrsim 2\pi/3$, where $k = 2\pi/\lambda$ and h is the shell thickness.[3] In agreement with classical linear analysis, we have observed significant finite shell thickness effects of the kind described here in our simulations in the range $1/3 < k\Delta x < 3$. The nonlinear analysis of the effects of finite thickness and the transition to nonlinear behavior in terms of A/λ and A/h for an ideal fluid layer falling freely under gravity will be reported elsewhere. From the slopes of the dashed curves in Figs. 8 and 9 it is apparent that the linear growth rates of the unstable modes illustrated are equal, but the amplitude at which nonlinear behavior is evident (departure from the dashed curves) is not the same although the initial perturbation wavelengths are identical.

From Figs. 9 and 11 it is seen that the shell thickness at the bubble center has the same value when departure from linear growth occurs. It is important to note that transition to nonlinear mode evolution occurs not at A/λ_y values near 0.4, as observed for ideal semi-infinite mass fluid layers,[16] but at lower values for a finite thickness shell (here $k\Delta x \sim 1$). For the cases of Fig. 8, nonlinear behavior occurs for $A/\lambda_y \simeq 0.2$ and 0.1 for initial values of $A/\lambda_y = 0.1$ and 0.03, respectively. For the higher irradiance case (Fig. 9), nonlinear transition occurs at $A/\lambda_y \sim 0.2$ and 0.1 for the same initial values of A/λ_y, viz., 0.1 and 0.03, in approximate agreement with the results of the lower-irradiance case. The increased growth times to amplitudes of the order of the shell thickness (or enhanced shell lifetimes prior to ablative rupture) observed to be due to nonlinear mode evolution may perhaps be useful for fusion target design, but attention to nonlinear mode-mode interactions is required to quantitatively exploit this conjecture.

I. Effects of wavelength

The nearly identical linear growth rates of longer wavelength modes may be of concern, in light of our conclusion that the longer wavelength mode is the more globally disruptive of the two wavelengths considered. The authors of Ref. 9 also arrived at a similar conclusion in their consideration of the effect of mode wavelengths. From Fig. 3, we choose two longer wavelengths (3.0 μm and 3.5 μm) and one intermediate wavelength (1.5 μm), which is located near the relative maximum is the $\gamma(k_y)$ spectrum, in order to illustrate that our conclusions based on the 1.0 μm and 2.5 μm simulations are of general applicability. In Fig. 12 we plot the simulation results for the mode amplitudes for all five wavelengths. Note that there is little difference in the nonlinear evolution of the two longer wavelength amplitudes when compared to the 2.5 μm case. Also note that the shortest wavelength considered (1.0 μm) represents a mode on the decreasing (large k) side of the linear growth curve (Fig. 3) where initial amplitude effects are not as important as for the longer wavelength modes, as predicted by linear theory. The 1.0 μm case is important in that it illustrates that spike burn-off does not stabilize the mode. The 1.5 μm case represents decreased growth compared with the longer wavelength modes and

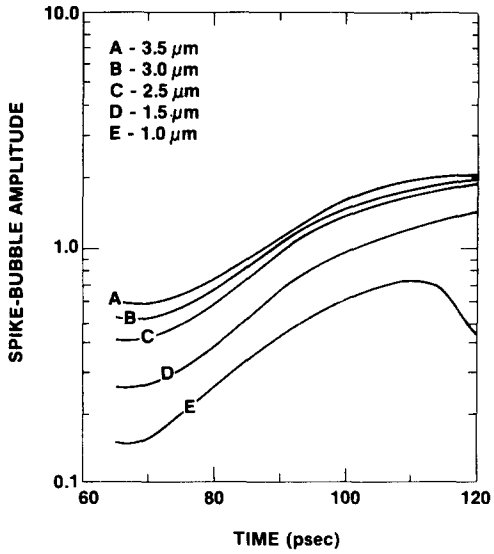

FIG. 12. Time evolution of spike amplitude for five different perturbation wavelengths for a carbon slab irradiated at 10^{15} W/cm^2. Note from the linear growth rate spectrum (Fig. 3) that both longer and shorter wavelengths than the 1.5 μm ($k = 4.2 \times 10^4$ cm^{-1}) case corresponding to the local maximum in the $\gamma(k)$ spectrum are represented. The largest unstable amplitudes occur for the longer wavelengths.

does not result in spike burn-off. Furthermore, it is clear from Fig. 12 that this case is less disruptive than the longer perturbation wavelength cases considered. For this reason, it is apparent that the 1.0 μm and 2.5 μm modes used to illustrate most of the physical effects discussed in this section are representative of the behavior of the disruptive effects due to both long and short wavelength perturbations. We reiterate the need to obtain the linear growth curve (e.g., Fig. 3) for a given target composition and irradiance to identify the range of wavelengths of importance.

J. Conclusions

In summary, our results for the single frequency unstable cases show: (1) The center-of-mass motion of the shell is virtually unchanged by the presence of the Rayleigh–Taylor unstable structure. (2) For the laser irradiances considered, a laminar structure of both the front and back surfaces of the shell is observed. (3) Unstable modes continue to evolve in the nonlinear regime and result in decreased shell thickness in the region of the bubble center compared with the unperturbed ablated shell thickness. (4) A finite amplitude effect due to the ablation process shows that the amplitude-to-wavelength ratio (A/λ_y) at which the departure from linearly unstable growth occurs decreases as a function of the initial value of A/λ_y for the perturbation. Consequently, the rate at which the shell thins in time depends on the initial A/λ_y. This shows that improved surface fabrication can lead to larger shell lifetimes for a fixed shell aspect ratio. (5) The most globally disruptive single frequency modes are those for which $k\Delta x$ is of order unity ($k\Delta x \simeq 1.3$ for the 2.5 μm case and $k\Delta x \simeq 3$ for the 1.0 μm case). (6) Larger ablation rates (resulting from higher absorbed irradiances) can extend the effective aspect ratio of a shell before ablative rupture due to nonlinear mode evolution occurs, but at the expense of hydrodynamic efficiency.

III. RAYLEIGH–TAYLOR UNSTABLE FLOW FOR A FINITE THICKNESS IDEAL FLUID LAYER

Some insight into the nature of the flows discussed above is obtained by comparing our ablative results with those obtained by a very efficient numerical technique[11,12] to study the Rayleigh–Taylor instability of inviscid, incompressible, layered flows. The latter method relies on the representation of the density interface between two ideal incompressible inviscid fluids as a velocity dipole layer across which the fluid velocity has a continuous normal component but a discontinuous tangential component. The numerical procedure uses an iterative technique to obtain a solution of the integro-differential equations describing the interfacial motion. The derivation of the dipole sheet evolution equations for a fluid layer are given in Appendix B.

From our observation that Kelvin–Helmholtz roll-up does not occur (e.g., Fig. 5), we consider only the Atwood ratio, $\alpha = 1$ [see after Eq. (B14)] case, i.e., a fluid layer in vacuum for a finite fluid layer. We do not claim that roll-up cannot occur in ablatively accelerated targets; indeed we would expect such behavior if the irradiances were significantly lower than those used in this paper because the density gradients would tend to be smaller and mass convection rates lower near the ablation surface. Additional research is required to determine, quantitatively, the behavior of the lower-irradiance cases. The choice $\alpha = 1$ conveniently avoids Kelvin–Helmholtz roll-up in the ideal fluid calculations.

Results obtained using these techniques are presented in Fig. 13 for a semi-infinite fluid layer [Fig. 13(a)] and for a fluid layer of finite depth [Fig. 13(b)]. Both calculations are performed in units for which the wavelength $\lambda = 2\pi$, and a constant force per unit mass, $g = 1$, is directed along the negative y axis. The disturbance of the lower interface is given by $y = -0.02\pi \cos x, A/\lambda = 0.01$. Time t is measured in units of $(2\lambda/\alpha g)^{1/2}$ where $\alpha = 1$. In Fig. 13(a), plotted when the familiar nonlinear bubble and spike structure is apparent and the spike amplitude is near 5, $t = 3.025$. In Fig. 13(b), $t = 5.02$, when the spike is of the same amplitude as in Fig. 13(a).

It can be seen that there are large differences between the two cases. In the finite fluid layer, Fig. 13(b), the bubble velocity is actually decreasing at the time illustrated, in contrast to the constant bubble rise velocity which results in the semi-infinite fluid case, Fig. 13(a). Note that the finite fluid layer exhibits a broader, flatter bubble than that observed for a semi-infinite layer, and more nearly resembles the bubble structure seen in the DAISY simulations. The nature of the late-time evolution of the ideal fluid layer remains to be investigated.

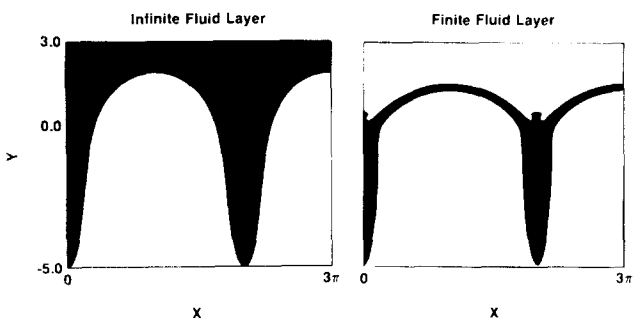

FIG. 13. Plot of the interface(s) of the $\alpha = 1$ Rayleigh–Taylor instability of layered flow of an ideal fluid. On the left, we plot the case for an unstable semi-infinite fluid layer interface at a late time $[t \equiv (2\lambda/\alpha g)^{1/2} = 3.025]$. Note that the nonlinear "bubble and spike" structure of the mode is fully developed. Plotted on the right is the instability of a finite ideal fluid layer (initial thickness unity), at $t = 5.02$ when the spike amplitude is nearly the same magnitude as for the semi-infinite case.

The anti-spike behavior evident in the final frame of the DAISY i-line mesh plot (Fig. 14) is a prominent feature of the large amplitude nonlinear evolution of the unstable finite fluid layer. In contrast to full mesh plots (see Fig. 2), i-line plots are obtained by plotting the grid lines which are initially in the plane of the unperturbed slab target (i.e., those lines nearly parallel to the y axis in Fig. 2), deleting the other two families of grid lines. The i-lines illustrate the distortion of the slab and are easier to follow, at the expense of omitting some information. Additionally, i-line plots illustrate ablative mass removal from the slab surface (or jetting of mass from the rear surface) because the mass between successive i-lines is constant in all the calculations presented in this paper. It can be seen that Fig. 13(a) corresponds, in an approximate way, to the 1 μm case (Fig. 4), where no anti-spike is observed in the density contours and the bubble is seen to be rounder than in the longer wavelength case (Fig. 5). The results plotted in Fig. 13(b), the finite fluid layer case, correspond approximately to the 2.5 μm case (c.f. Figs. 5 and 14).

In Fig. 15 we illustrate the time evolution of a unit thickness unstable finite fluid layer. The initial A/λ for this mode is -0.02. The time evolution of the spike closely resembles temporal spike evolution of the DAISY simulation shown in Fig. 14. The agreement is qualitative because the initial $A/\lambda_y = 0.1$ value for Fig. 14 is considerably larger

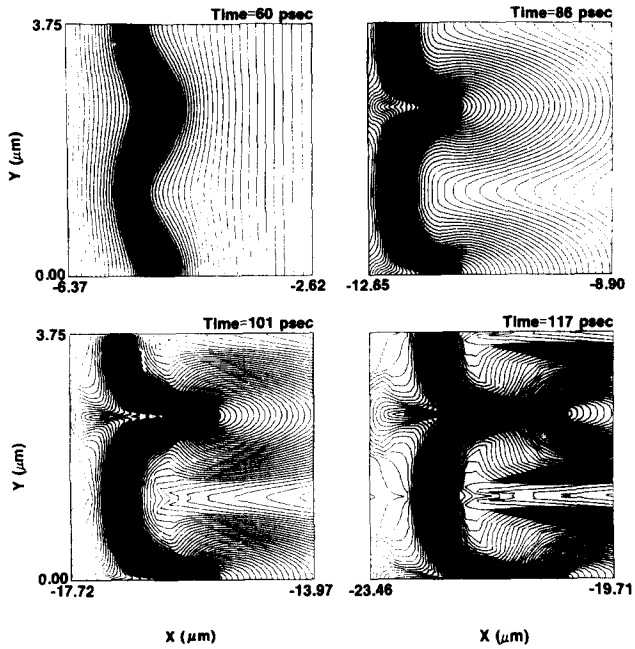

FIG. 14. DAISY "i-line" mesh plots illustrating the evolution of the 2.5 μm $A/\lambda_y = 0.1$) perturbation, for the 10^{15} W/cm^2 example whose density contours are illustrated in Fig. 5. Note the anti-spike apparent at 117 psec.

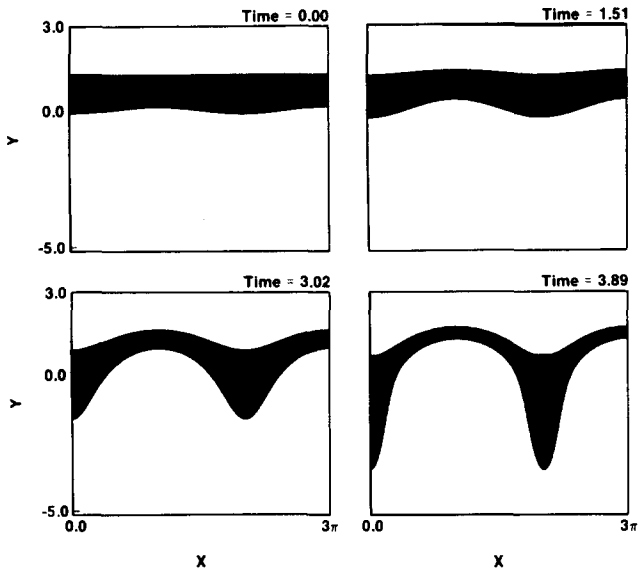

FIG. 15. Time evolution of the unit thickness finite layer Rayleigh–Taylor instability before formation of the anti-spike. Initially $A/\lambda = -0.02$ for this example.

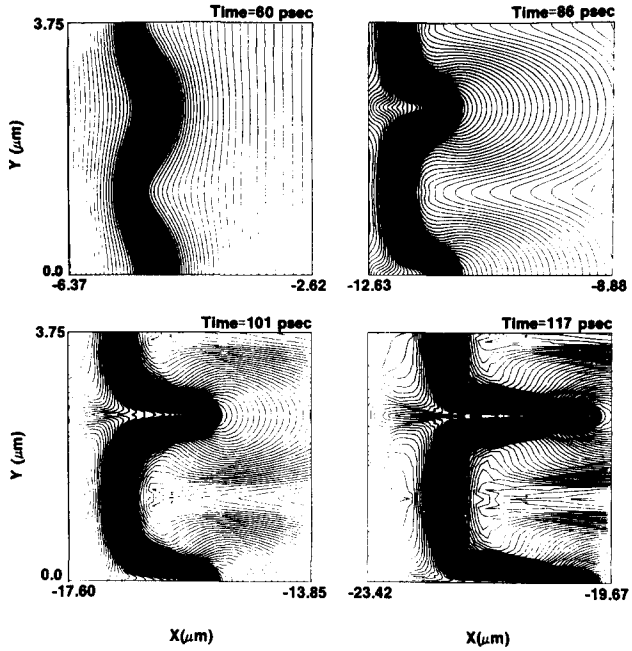

FIG. 16. DAISY "i-line" mesh plot of a two-frequency Rayleigh–Taylor instability. $\lambda_1 = 2.5\ \mu$m and $\lambda_2 = 1.25\ \mu$m, with $A_1/\lambda_{y_1} = 0.1$ and $A_2/\lambda_{y_2} = -0.025$. The simulation irradiance is 10^{15} W/cm^2.

than that of the ideal fluid layer illustrated in Fig. 15. This difference is to be anticipated due to the larger linear classical growth rate of an $\alpha = 1$ instability which is apparent in Fig. 3; The ideal fluid more rapidly approaches an amplitude to wavelength value of 0.1 by linearly unstable growth than does its ablative analog.

The similarities between the large-amplitude structure of unstable layered flow for an ideal fluid and our full two-dimensional simulations is exploited further in the next section. Here, we emphasize the similarities between the DAISY simulation results and the classical results for $\alpha = 1$. At the conclusion of the following section, we suggest how quantitative results from the boundary integral technique may be applied to the ablative cases of interest in inertial fusion research.

IV. NONLINEAR EVOLUTION OF THE MULTIFREQUENCY RAYLEIGH–TAYLOR INSTABILITY

We now consider multifrequency unstable Rayleigh–Taylor flow. We begin by pointing out that a universal parameter characterizing the multifrequency Rayleigh–Taylor instability does not appear to exist,[26] so each case must apparently be analyzed separately, even for a semi-infinite ideal incompressible fluid. There is an additional complication in the ablative compressible cases due to the finite amplitude effects associated with the finite shell thickness discussed in the previous section. However, by considering a series of these multifrequency cases, it is possible to identify the most serious ones. A comparison of the simulation results with the inviscid incompressible results suggests how to identify the potentially most disruptive failure modes for the cases of interest in designing ablatively driven laser fusion targets.

In Figs. 16 and 17 we show the simulation results for the ablative case for a two-frequency Rayleigh–Taylor unstable flow where the wavelengths and initial amplitudes of the two modes are 2.5 μm and 1.25 μm and $A/\lambda_y = 0.1$ and -0.025 ($kA = \pi/5$ and $-\pi/20$), respectively. It can be seen by comparison with Fig. 14 that there is a dramatic difference in the nonlinear evolution due to the addition of the shorter wavelength, and the spike now contains a larger amount of material when compared with the single frequency resulted plotted in Fig. 14. The density contours for this case (Fig. 17) best illustrate this effect. Note that the bubble region if flatter than that of Fig. 5, and the broader spike contains a relatively larger portion of the shell mass.

Figure 18 shows results for a two-frequency Rayleigh–Taylor unstable case obtained using the boundary integral

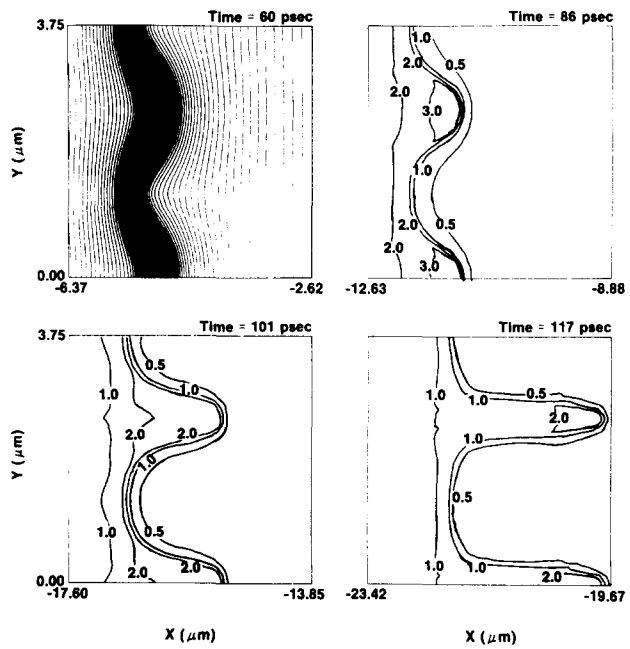

FIG. 17. DAISY "i-line" mesh configuration at initialization, and time evolution of the density contours for the $I = 10^{15}$ W/cm^2 two-frequency simulation of Fig. 16.

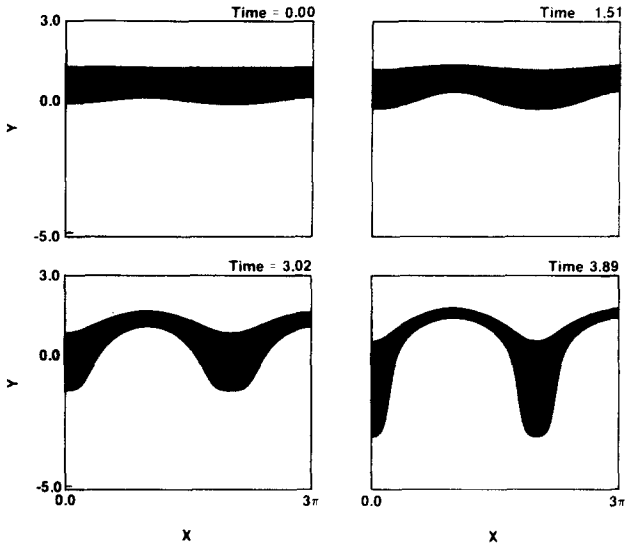

FIG. 18. Time evolution of the two-frequency instability of a unit thickness ideal fluid layer. Here $\lambda_1 = 2\pi$, $\lambda_2 = \pi$ and $A_1/\lambda_1 = -0.02$, $A_2/\lambda_2 = 0.005$. Compare the mode structure with that of the single-frequency example illustrated in Fig. 15.

technique for an inviscid incompressible fluid with $A/\lambda = -0.02$ and 0.005 initially for the two modes. Note that the addition of a second wavelength of very small amplitude in the ideal fluid case leads to the same qualitative behavior of a broader spike containing a larger shell mass fraction (compare Figs. 15 and 18).

An important consequence of the two-frequency instability concerns the behavior of the shell thickness as a function of time as illustrated in Fig. 19 for the irradiance $I = 10^{15}$ W/cm^2 used in Sec. II. The solid line in Fig. 19 is the same as the solid curves in either Fig. 7 or Fig. 11 of the previous section; the lower broken line, obtained for the two-frequency case, illustrates the effect of decreased shell lifetime for the multi frequency mode. The shell thins much more rapidly in the two-frequency case than in the single-frequency case.

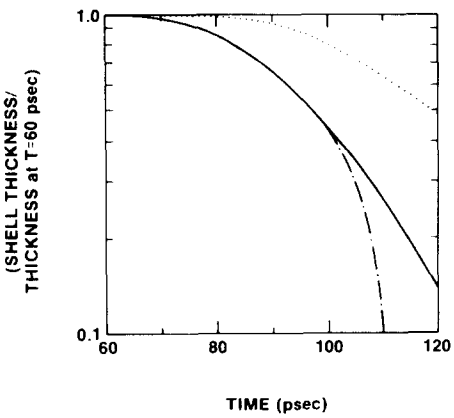

FIG. 19. Shell thickness (c.f. Fig. 7) at the bubble center as a function of time for the 10^{15} W/cm^2 DAISY simulations. Solid curve: the single-frequency perturbation with $\lambda_y = 2.5$ μm ($A/\lambda_y = 0.1$). Dashed curve: the two-frequency perturbation ($\lambda_1 = 2.5$ μm, $\lambda_2 = 1.25$ μm, with $A_1/\lambda_{y_1} = 0.1$, $A_2/\lambda_{y_2} = -0.025$). Dotted curve: evolution of the unperturbed shell thickness.

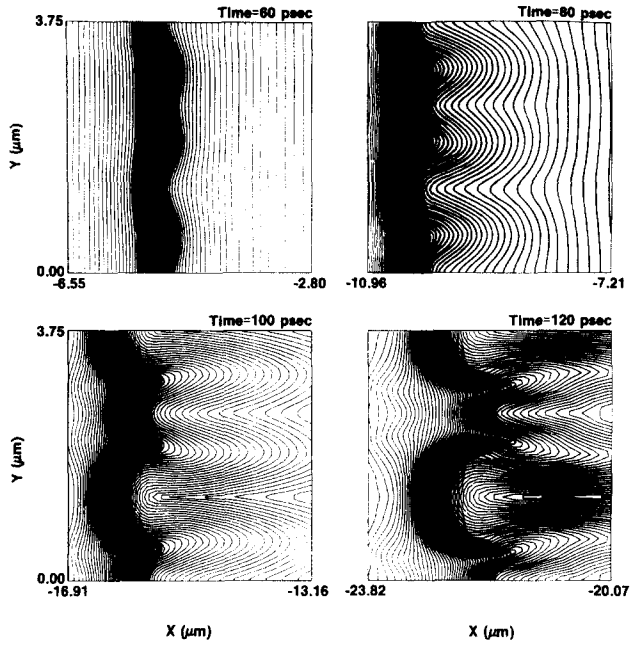

FIG. 20. DAISY "i-line" mesh plots illustrating the two-frequency perturbation ($\lambda_1 = 2.5\,\mu$m, $\lambda_2 = 1.25\,\mu$m) where the initial amplitude-to-wavelength ratio of the harmonic is large compared to the fundamental ($A_1/\lambda_{y_1} = 0.025$, $A_2/\lambda_{y_2} = -0.05$). The absolute initial amplitudes of each mode are equal. Note the growth of the bubble due to the harmonic in the spike of the fundamental.

Figures 20 and 21 illustrate a two-frequency Rayleigh–Taylor mode where A/λ_y for the shorter wavelength has now been increased by a factor of two to -0.05. It can be seen that the second frequency contributes by effectively opening up the spike of the fundamental (longer wavelength) mode, and results in more mass motion out through the spike into the higher temperature region where it is ablated away. The density contours shown in Fig. 21 best illustrate

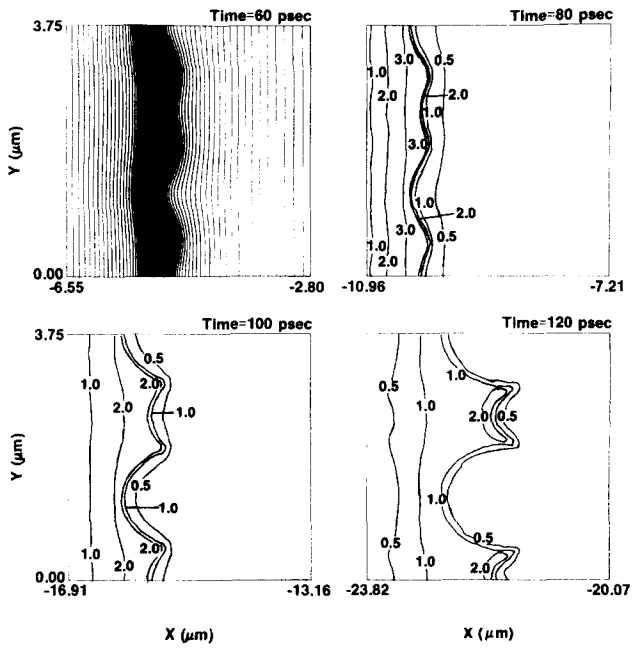

FIG. 21. Initial DAISY "i-line" mesh configuration at initialization and time evolution of the density contours for the $I = 10^{15}$ W/cm^2 two-frequency simulation of Fig. 20.

the enhanced mass now associated with the spike region by comparison with Fig. 5. Figure 22 illustrates that a similar effect is observed for the incompressible ideal fluid. In Fig. 22, we have increased the absolute value of the initial amplitude-to-wavelength ratio, A/λ, for the harmonic wavelength from 0.005 to 0.01. Note that the harmonic bubble appearing in the spike appears in this case in analogy with the effect seen in the full simulations (see Figs. 16, 20 and compare with Figs. 18 and 22), where the initial harmonic amplitude of the second mode was changed by the same ratio.

One conclusion from this comparison is that the behavior of the multifrequency instability is sensitive to the relative amplitude-to-wavelength ratios of the modes considered for a given shell thickness. Secondly, a comparison of mode structure between the full simulation cases and the ideal fluid cases illustrates that it is the relative amplitude between the fundamental and the harmonic for a finite thickness shell that determines the complicated bubble and spike structure. This second result is the one we wish to exploit.

In Figs. 23 and 24 we show a two-frequency result (the wavelengths illustrated are now 2.0 μm and 1.0 μm with $I = 10^{15}$ W/cm^2 as before), where we have picked a large initial amplitude of the second harmonic [$A/\lambda_y = 0.05$ and -0.10 for the fundamental (2.0 μm) and harmonic (1.0 μm) wavelengths, respectively]. The evolution of instability exhibits evidence of mode coalescence. If one plots the spike location of the short wavelength as a function of time, it convects toward the location of the spike due to the fundamental (longer wavelength) mode. The effect of such a coalescence does not tend to increase shell lifetime.

The tendency of the multifrequency instability to enhance shell failure as judged by the shell thinning rate can be seen in Fig. 25 for the three ablative examples of the two-frequency cases we have discussed. Of the three cases illustrated, it can be seen that the harmonic frequency acts to decrease the lifetime of the shell over that due to the single frequency case alone. In particular, note that for a fixed initial value of A/λ_y for the fundamental mode (curves B, C of Fig. 25), increasing the initial A/λ_y of the harmonic results in shorter shell lifetime. This result is part of the two-frequency instability analog of the finite initial amplitude effect discussed in Sec. II. Additionally, for a fixed relative A/λ_y for the fundamental and harmonic, note that larger initial amplitudes also result in shorter shell lifetimes (compare curves A and C of Fig. 25).

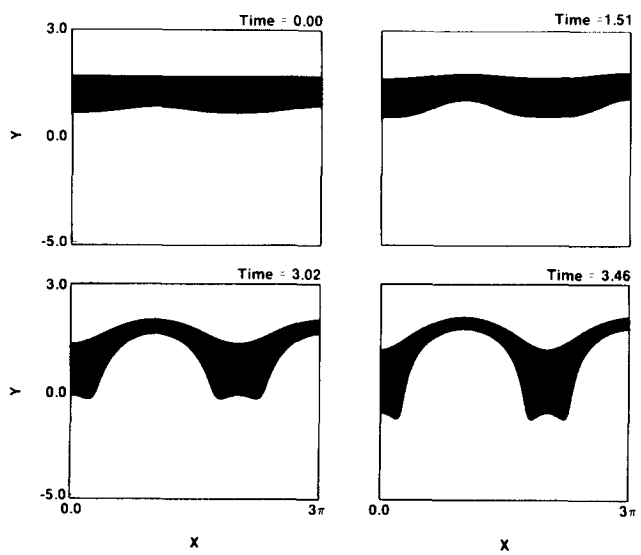

FIG. 22. Time evolution of the two-frequency instability of a unit thickness ideal fluid layer with an enhanced harmonic initial amplitude. In this example $\lambda_1 = 2\pi$, $\lambda_2 = \pi$ and $A_1/\lambda_1 = -0.02$, $A_2/\lambda_2 = 0.01$.

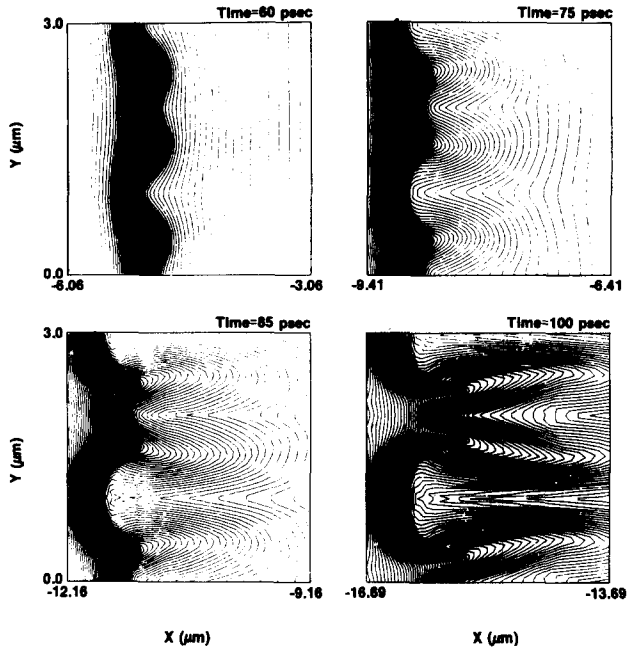

FIG. 23. DAISY "i-line" mesh plots illustrating a two-frequency instability with a harmonic initial amplitude large compared to the fundamental. In this example $\lambda_1 = 2.0$ μm, $\lambda_2 = 1.0$ μm with $A_1/\lambda_{y_1} = 0.05$, $A_2/\lambda_{y_2} = -0.1$. The irradiation is 10^{15} W/cm^2. Note the evidence of mode coalescence by comparing the bubble width which appears at the fundamental spike location at 75, 85, and 100 psec. The same type of coalescence can also be seen in Fig. 20.

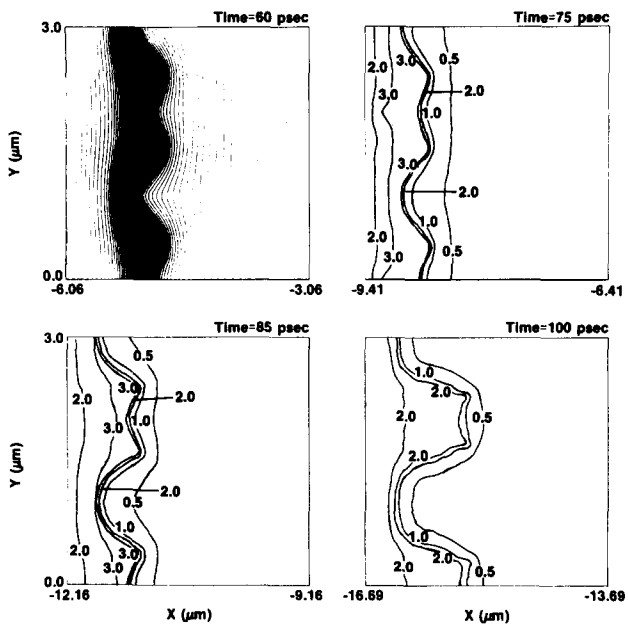

FIG. 24. DAISY "i-line" mesh configuration at initialization and the time evolution of the density contours for the two-frequency instability of Fig. 23.

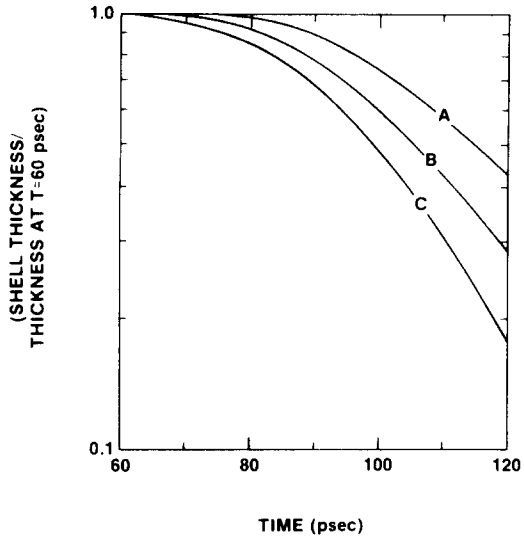

FIG. 25. Shell thickness (as in Fig. 7) at the bubble center as a function of time for two-frequency DAISY simulations with $\lambda_1 = 2.5\,\mu$m and $\lambda_2 = 1.25\,\mu$m, for different initial amplitudes: (A) $A_1/\lambda_{y_1} = 0.025$, $A_2/\lambda_{y_2} = -0.05$, (B) $A_1/\lambda_{y_1} = 0.05$, $A_2/\lambda_{y_2} = -0.05$, and (C) $A_1/\lambda_{y_1} = 0.05$, $A_2/\lambda_{y_2} = -0.1$.

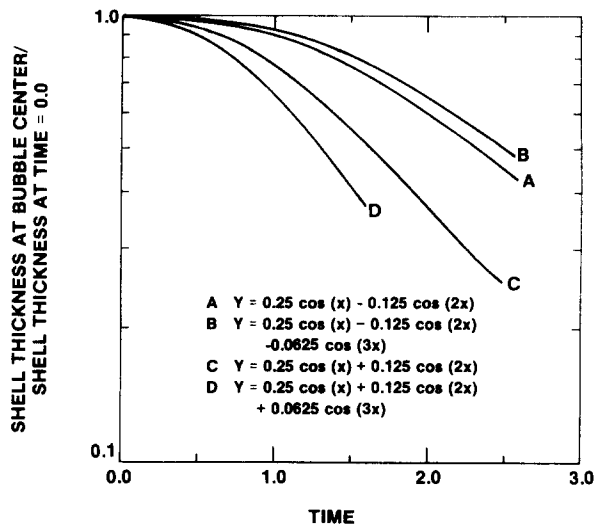

FIG. 27. Thickness at the bubble center as a function of time for two-frequency and three-frequency boundary integral calculations of an unstable finite ideal fluid layer of initially unit thickness. Note that the presence of the second harmonic out of phase with the fundamental has the largest relative effect on unstable shell thinning (compare A with C, B with D vs A and B or C and D).

This same qualitative observation can be made from Fig. 26 for the ideal fluid, where nonlinear mode evolution results in a more rapid thinning of the shell when compared with the single mode case (compare curves A and B of Fig. 26). Furthermore, note from the figure that enhancement of the shell thinning effects also results from larger initial values of A/λ for the harmonic (compare curves B and C of Fig. 26).

These effects, observed for an ideal fluid, are in direct analogy with the full DAISY simulation results for the two-frequency Rayleigh–Taylor instability. This agreement may have been anticipated by recalling that the Rayleigh–Taylor instability is a subsonic phenomenon, but the full simulations are required to determine the effective Atwood number for the ablative compressible case before the ideal fluid code can be effectively exploited. Nevertheless it is clear that the simulation results may be interpreted in terms of the classical nonlinear evolution of unstable modes for finite thickness fluid layers.

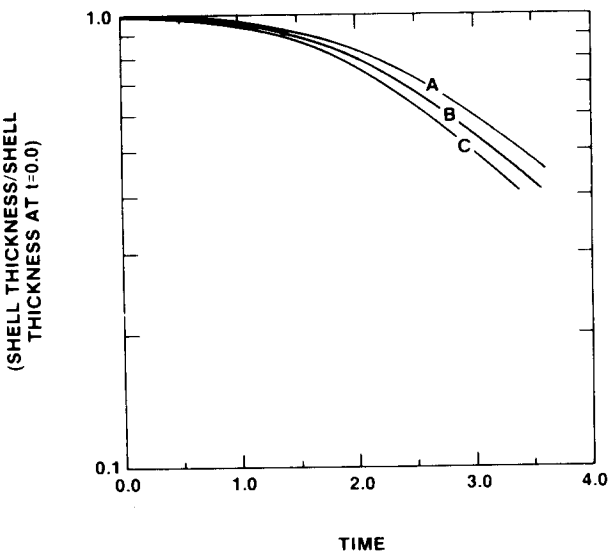

FIG. 26. Thickness at the bubble center as a function of time for various two-frequency ($\lambda_1 = 2\pi$, $\lambda_2 = \pi$) boundary integral calculations of an ideal fluid layer initially of unit thickness. (A) $A_1/\lambda_1 = -0.02$, $A_2/\lambda_2 = 0.0$, (B) $A_1/\lambda_1 = -0.02$, $A_2/\lambda_2 = 0.005$, and (C) $A_1/\lambda_1 = -0.02$, $A_2\lambda_2 = 0.01$.

There are two major differences between the ideal fluid and the ablative cases: (1) The linear growth rates for the ideal fluid layer tend to be larger by approximately a factor of two (see Fig. 3) than the ablative compressible linear growth rates in the range $1/3 < k\Delta x < 3$. (2) The ablative linear growth rate curve has a local maximum near $k\Delta x \sim 2$ compared with the monotonically increasing growth rates for an ideal fluid instability. The latter effect can be added to the ideal fluid model by the inclusion of a stabilizing term, such as surface viscosity without giving up the computational advantages of the boundary integral technique. However, classical Newtonian viscosity in the interior of the fluid cannot be used to reduce the growth rate as it gives rise to a diffusion of vorticity into the fluid interior and away from the boundary. The latter effect must be treated by solution of the full Navier–Stokes equations.

In the range $1/3 < k\Delta x < 3$, the ideal fluid calculations predict the most important effects of shell thinning and mode-mode interactions. It has been demonstrated that smaller kA values than those employed in the ablative simulations lead to quite similar nonlinear mode structures for both the single-frequency and two-frequency examples presented.

The boundary integral technique provide a useful tool for the simulation of the Rayleigh–Taylor instability of a randomly perturbed interface. In Fig. 27 we give a comparison of the results obtained for two two-frequency instabilities and two three-frequency instabilities. It can be seen from the figure that the presence of harmonics in the initial mode spectrum, which are out of phase with the fundamental, re-

sults in the largest relative shell thinning effect. That is, there is a larger shell thinning as a function of time between curves A and D (or B and C) than that observed between A and B (or C and D).

V. CONCLUSIONS

We have shown various effects of multi-wavelength unstable perturbations and demonstrated the utility of a boundary integral method to determine the effects of the multiwavelength and, ultimately, the random Rayleigh–Taylor problem for an ideal fluid layer. The boundary integral techniques introduced here can serve as a first-order estimate for the unstable ablative compressible problem.

Plots of the amplitude of an unstable fluid layer at its thinnest position as a function of time have shown that multiwavelength effects are most important for a combination of modes in the range $1/3 < k\Delta x < 3$. Although k values larger than those at the end of this range have enhanced linear growth rates in the classical case, the penetration depth of these modes is less and the modes are less globally disruptive. Furthermore, a full ablative determination of the unstable spectrum indicates that the effects of thermal conduction substantially reduce the growth rate for large k modes ($k\Delta x > 3$), and they are therefore not important in failure considerations for ablatively accelerated shells. By comparison with the full simulations, we have demonstrated that it is important to consider only a portion of the unstable spectrum to estimate the worst case effects.

We summarize our results as follows: (1) The multiwavelength results are consistent with the single-frequency results as regards the laminar structure observed for both the anterior and posterior surfaces of the shell for the laser irradiances simulated. (2) The addition of a second harmonic wavelength results in an increased rate of shell thinning when compared with the shell thinning rate of the fundamental mode alone. (3) Initial A/λ_y values are important in determining mode evolution; A/λ_y values of order of 0.1 or less for a mode result in the dominance of nonlinear effects. (4) Mode coalescence appears to occur but does not appear to result in decreased bubble rise velocities in a finite fluid shell. (5) The comparison of the classical inviscid incompressible results with the full ablative compressible simulations illustrates the qualitative agreement between the nonlinear evolution of these diverse Rayleigh–Taylor unstable modes. (6) During ablative motion, inflight aspect ratios as high as 40 may be used by going to higher irradiances, at the expense of hydrodynamic efficiency, before ablative rupture occurs.

The use of one-dimensional simulations to obtain the rate of shell thinning due to mass ablation can be used together with ideal fluid results which determine acceptable initial A/λ values for components of the unstable modes in the range $1/3 \lesssim k\Delta x \lesssim 3$. Shell-thinning effects, calculated using boundary integral techniques, due to the Rayleigh–Taylor instability alone give a first-order estimate of the enhanced rate at which an unstable ablatively accelerated shell will become thinner.

The thinning rates, as a function of time, should be measured in units of the classical growth rate. The number of growth times required for an unstable shell to reach a limiting thickness may then be used to estimate the effects of the instability in the ablative case by rescaling the resulting time in units of the ablative linear growth times (e.g., see Fig. 3). This procedure allows one to estimate an enhanced thinning time, to be subtracted from the thinning time due to ablation alone. This computationally efficient expedient significantly reduces the computer time required to assess the surface finish and shell irradiation uniformity requirements for the success of ablatively driven laser fusion pellets.

ACKNOWLEDGMENTS

This work was partially supported by the following sponsors: Exxon Research and Engineering Company, General Electric Company, Northeast Utilities, New York State Energy Research and Development Authority, The Standard Oil Company (Ohio), The University of Rochester, and Empire State Electric Energy Research Corporation. This work is also supported by the U. S. Department of Energy inertial fusion project under contract No. DE-AC08-80DP40124.

Major support for the boundary integral calculations was provided by the Theoretical and Applied Theoretical Physics Divisions of the Los Alamos National Laboratory of the University of California under contract to the United States Department of Energy. Partial support was given by the Office of Naval Research under Contract No. N00014-77-C-0138, and under Subcontract No. 9245009 with the Lawrence Livermore National Laboratory.

APPENDIX A: DAISY COMPUTATIONAL MODEL

In this Appendix, we summarize some of the unique features of the DAISY computer code. Several features of the DAISY code, in particular the formulation of electron thermal conduction on a distorted triangular mesh, are presented in some detail.

DAISY is a two-dimensional Lagrangian code which employs triangular zoning in cylindrical (R-Z) geometry. While Lagrangian codes have difficulty treating flows with significant distortion due to shear, they are particularly effective in treating flows with nonrigid boundaries or interfaces between fluids possessing different thermodynamic properties. Thus, the flows considered here are most effectively simulated on a Lagrangian rather then Eulerian grid. If large shear distortions, were present, remeshing algorithms[27,28] would be necessary in the Lagrangian DAISY code. However, no remeshing was requiring for the cases presented in this paper.

1. Hydrodynamics

The axisymmetric Eulerian equations for the flow of an inviscid compressible fluid in cylindrical geometry are:

$$\frac{\partial \rho}{\partial t} + u\frac{\partial \rho}{\partial r} + v\frac{\partial \rho}{\partial z} = -\rho\left(\frac{\partial u}{\partial r} + \frac{\partial v}{\partial z} + \frac{u}{r}\right), \tag{A1}$$

$$\frac{\partial u}{\partial t} + u\frac{\partial u}{\partial r} + v\frac{\partial u}{\partial z} = -\frac{1}{\rho}\frac{\partial P}{\partial r}, \tag{A2}$$

$$\frac{\partial v}{\partial t} + u\frac{\partial v}{\partial r} + v\frac{\partial v}{\partial z} = -\frac{1}{\rho}\frac{\partial P}{\partial z}, \tag{A3}$$

$$\frac{\partial E}{\partial t}+u\frac{\partial E}{\partial r}+v\frac{\partial E}{\partial z}=-P\left(\frac{\partial V}{\partial t}+u\frac{\partial V}{\partial r}+v\frac{\partial V}{\partial z}\right), \tag{A4}$$

$$P=P(V,E) \tag{A5}$$

where u is velocity in the radial (r) direction, v the velocity in the axial (z) direction, ρ the fluid density, P the fluid pressure (due to ions and electrons), E the fluid specific internal energy, and V the fluid specific volume ($1/\rho$).

Lagrangian equations result from a change of variables from the Eulerian coordinates (r,z,t) to the Lagrangian coordinates (R,Z,t'). The transformation of the derivatives,

$$\left.\frac{\partial}{\partial r}\right|_{z,t},\quad \left.\frac{\partial}{\partial z}\right|_{r,t},\quad \left.\frac{\partial}{\partial t}\right|_{r,z}$$

(where the quantities to the lower right of the vertical bar are those which are held fixed) appearing in the Eulerian equations are obtained using the Jacobian,

$$J=\frac{\partial(r,z,t)}{\partial(R,Z,t')}=\frac{\partial(r,z)}{\partial(R,Z)},$$

where we have used $t'\equiv t$. Making the Lagrangian identifications $\partial R/\partial t=u$ and $\partial Z/\partial t=v$, one obtains:

$$\left.\frac{\partial}{\partial t}\right|_{r,z}+\mathbf{U}\cdot\nabla=\left.\frac{\partial}{\partial t}\right|_{R,Z},$$

where

$$\mathbf{U}\equiv u\hat{e}_r+v\hat{e}_z,$$

where $\hat{e}_{r,z}$ are unit vectors in the r and z directions, respectively. The transformation of the continuity equation (A1) yields

$$\rho/\rho_0=\Omega_0/\Omega, \tag{A6}$$

where ρ_0 and Ω_0 represent the cell density and volume, respectively, at time $t=0$. The Lagrangian momentum equations. (A2) and (A3) result in the radial and axial accelerations:

$$a_R=-\frac{1}{\rho}\frac{\partial P}{\partial r}=-\frac{1}{\rho_0}\left(\frac{\partial P}{\partial R}\frac{\partial z}{\partial Z}-\frac{\partial P}{\partial Z}\frac{\partial z}{\partial R}\right)\frac{r}{R}, \tag{A7}$$

and

$$a_Z=-\frac{1}{\rho}\frac{\partial P}{\partial z}=\frac{1}{\rho_0}\left(\frac{\partial P}{\partial R}\frac{\partial r}{\partial Z}-\frac{\partial P}{\partial Z}\frac{\partial r}{\partial R}\right)\frac{r}{R}. \tag{A8}$$

The energy equation (A4) becomes

$$dE=-PdV. \tag{A9}$$

We now summarize the finite difference form of Eqs. (A6) through (A9) on the DAISY computational mesh.

Figure 28 represents the basic computational grid used in DAISY. The simulation proceeds using discrete zones, each of which has fluid thermodynamic and kinematic properties associated with it. The DAISY triangular zones lie in the RZ plane, each representing a torus about the Z-axis. Thermodynamic quantities, e.g., pressure, density, or temperature, are defined at the triangle centroids and are assumed constant through the entire triangle. Kinematic quantities, e.g., acceleration, velocity, R and Z positions are defined at vertex points indicated by the black dots in Fig. 28. Each vertex point, referred to as an inertial mass point in DAISY has an index marker (I,K) which labels the zone on the two-dimensional Lagrangian grid. The zone accounting logic used in

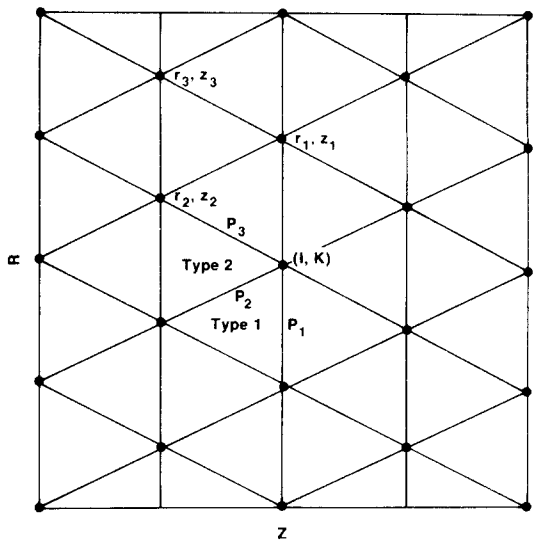

FIG. 28. DAISY computational mesh.

DAISY assigns two additional quantities to each vertex point. The zone type (1 and 2 as illustrated in Fig. 28) is stored separately. Each vertex point also has three panels P1, P2, and P3 (see Fig. 28) associated with it. Thus, conservation of mass [Eq. (A6)] becomes

$$\rho_{(I,K)}=\rho_{0(I,K)}\Omega_0(I,K)/\Omega(I,K). \tag{A10}$$

The volume of a triangular zone $\Omega(I,K)$ is given by

$$\Omega_{(I,K)}=\bar{r}_{c(I,K)}A_{(I,K)}\ \text{(per radian)},$$

where $\bar{r}_{c(I,K)}$ is the area centroid for zone (I,K) and $A_{(I,K)}$ is the zone (I,K) cross-sectional area in the RZ plane.

The treatment of the momentum equation, Eqs. (A7) and (A8), is more complicated. The dynamic variables are located at the inertial mass points (vertices) of a zone. There are six zones surrounding a given inertial mass point and six panels emanating from each inertial mass point across which pressure differences can exist. The radial and axial accelerations at each inertial mass point are obtained by determining the R and Z components of the total force acting at each inertial mass point and then dividing by the mass associated with the point. The mass can be obtained in a variety of ways, but the simplest is to use the mass associated with the volume obtained by connecting the area centroids of the six surrounding zones, as illustrated in Fig. 29.

The force on a given panel is obtained by assuming that the pressure difference between two adjacent zones acts uniformly along the panel separating the two zones. The resultant force distribution due to the pressure difference across a panel then results from linear interpolation along the panel. The velocity and displacements for a given point are obtained by intergrating the Lagrangian equations of motion explicitly in time:

$$\frac{du}{dt}=a_R,\quad \frac{dv}{dt}=a_Z, \tag{A11}$$

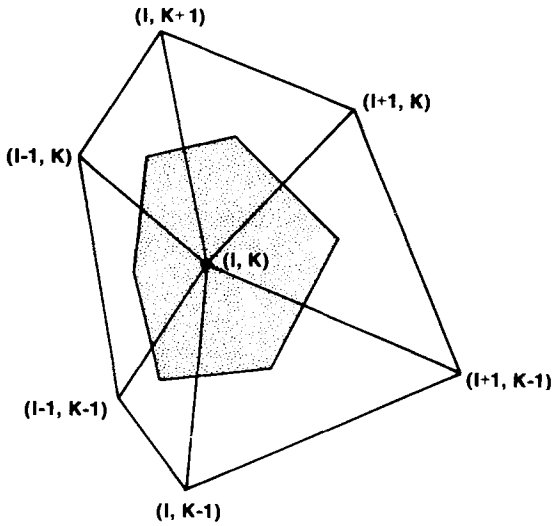

FIG. 29. Inertial mass determination scheme on the DAISY mesh.

and

$$\frac{dR}{dt} = u, \quad \frac{dZ}{dt} = v.$$

Once new positions (densities) have been calculated, the results can be used to obtain the new internal energy and pressure in each zone, Eqs. (A9) and (A5), if there is no additional energy transport from other processes.

In order to treat shock discontinuities, we use the familiar Richtmyer–von Neumann[29] method of adding an artificial viscous pressure term in Eqs. (A7)–(A9). A number of different expressions has been developed for artificial viscosity in multidimensional hydrodynamics.[30–32] After investigation of several forms we found that the artificial viscosity (q) most satisfactory for DAISY to be similar in form to that suggested by von Neumann and Richtmyer:

$$q = (a^2/V)(v_\perp)^2, \tag{A12}$$

where $a^2 = \text{const.}$ and $v_\perp$ is the maximum velocity of the inertial mass point along a perpendicular from the inertial mass point to the opposite panel in the frame where the centroid is at rest.

If a zone is expanding (decreasing density), $q = 0$ is used. For a zone whose density is increasing, a further check required in converging geometries is performed. The maximum perpendicular velocity used in Eq. (A12) must have a component across the zone. The q term is assumed constant over an entire zone and added to the pressure to calculate Eqs. (A7)–(A9).

Some of the virtues of triangular zoning have been incorporated into quadrilateral codes by the use of triangular subzoning.[33] Frequently, difficulties are encountered when simulating oblique shocks passing through quadrilateral grids containing long thin zones. P. L. Brown and K. B. Wallick have shown that by breaking a quadrilateral zone into four triangular subzones more physically realistic behavior can be obtained.[33] For a shock entering a zone that is subzoned, the artificial viscous pressure, as well as the energy change associated with the shock heating, is confined locally to those triangles in the affected region.

The treatment of hydrodynamic boundary conditions in DAISY is accomplished without any special treatment of the momentum equations at boundaries. The momentum equation requires vertex point positions, velocities, and a zone-centered pressure. Nonrigid boundaries are treated by assuming the pressure is zero (or prescribed in some applications) in the region outside the fluid computational mesh. Once the pressure outside the computational mesh is determined, all quantities necessary to evaluate Eqs. (A7) and (A8) are known. Nonrigid boundaries do not require extension of the computational grid, just the storage of the external pressure.

Slip surfaces, surfaces along which one component of the velocity is zero for all time, are handled without changes to the momemtum equation algorithm. The slip surface is obtained by setting the desired components of the acceleration at such a surface to zero for time $t \geqslant 0$.

2. Electron thermal diffusion

The energy conservation equations used in DAISY result from the first law of thermodynamics using

$$\dot{E} + p\dot{V} = \dot{S}, \tag{A13}$$

where $\dot{E}$ is the rate of increase of the internal energy of the system, $p\dot{V}$ the rate at which work is done on the system, and $\dot{S}$ is the rate at which heat is entering the system.

The internal energy E can be written as a function of V and T, where T is the temperature:

$$C_v \frac{\partial T}{\partial t} + \left(P + \frac{\partial E}{\partial V}\bigg|_T\right)\frac{\partial V}{\partial t} = \frac{\partial S}{\partial t}, \tag{A14}$$

where C_v is the specific heat at constant volume. For a single species system, S includes diffusion of heat from one point to another by thermal conduction, sources in the system (e.g., laser energy deposition), and radiative losses.

Including electron thermal diffusion and the sources Eq. (A14) becomes:

$$\rho C_v \frac{DT}{Dt} = \nabla\cdot(\kappa\nabla T) + S', \tag{A15}$$

where $\dot{S}'$ is the external source plus the work, and κ is the thermal conductivity.

The difficulty in applying Eq. (A15) on a distorted mesh is the construction of accurate heat fluxes arising from the gradient (∇T) term.

The method used in DAISY consists of a combination of both finite difference and methods more closely related to finite elements. Referring to Fig. 30, temperatures in a zone are defined at the area centroid and at the three vertex points. The temperature at a vertex point is defined as the average of the centroid temperatures of the six surrounding zones. Other weighting schemes for determining the vertex point temperature, such as angle or area weighting, have been used. For the simulations presented in this paper, we found that the added complexity of these alternative schemes was not warranted because they did not significantly change the results of comparison test cases. The temperature is assumed to vary linearly between a centroid and a vertex point. The temperature gradient across a given panel is found by determining the temperatures where the perpen-

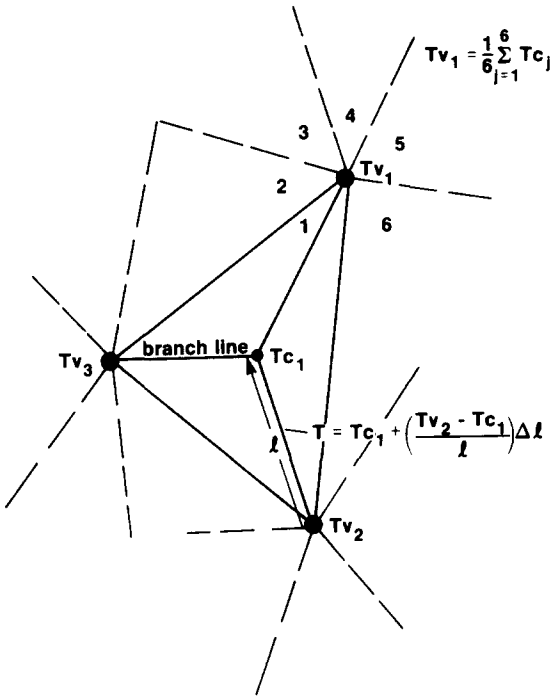

FIG. 30. Vertex and centroid temperatures on the DAISY mesh.

dicular bisector of a panel intersects a temperature branch line (see Fig. 31) and then dividing the difference by the distance separating the two intersection points. The form of the temperature gradient depends upon which branch lines the panel perpendicular bisector intersects. There are four such possible cases.

The numerical stability time step limit imposed by the diffusion equation may be many orders of magnitude smaller

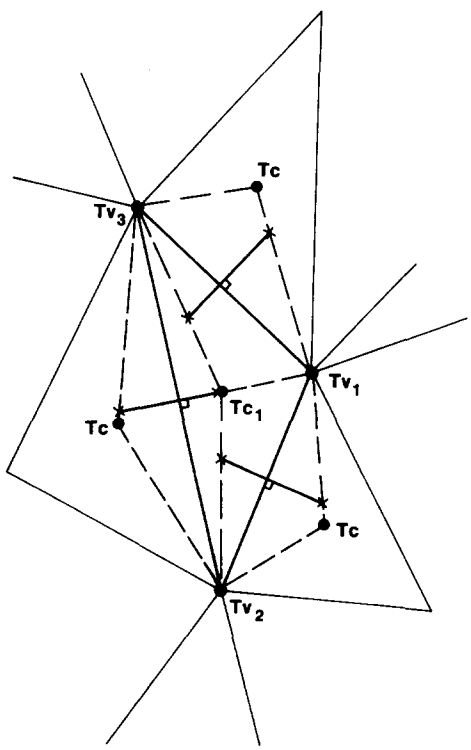

FIG. 31. Interpolation procedure for temperature gradients in DAISY.

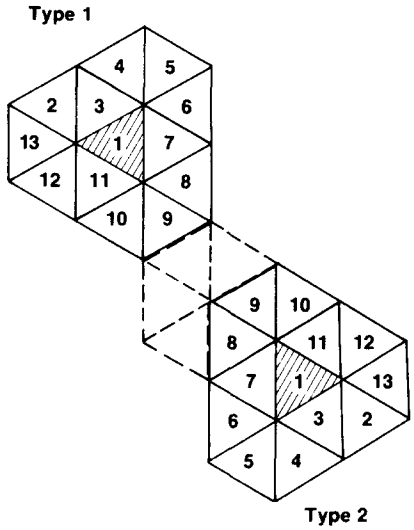

FIG. 32. Combinations of neighboring zones contributing to the heat flux for a Type 1 or Type 2 triangular DAISY zone.

than that required by the hydrodynamic equations. The severity of this restriction [Eq. (A15)] requires an implicit time stepping procedure.

In analogy with the DAISY hydrodynamics, there are two types identifiers associated with a given (I,K) point. Each zone, depending on whether it is a type 1 or type 2, has a slightly different combination of corner zones which determine the temperature gradient. Referring to Fig. 32, there are thirteen possible triangles which can enter in the calculation of the heat flux for an individual triangle. However, due to topological differences in triangle types, the resulting matrix equation to be solved in an implicit formulation has fifteen nonzero diagonals. The solution of a matrix this size [$NM \times NM$ where $N(M)$ is the number of zones in $Z(R)$] by means of matrix inversion techniques such as Incomplete Cholesky Conjugate Gradient Methods[34] (ICCG) was found too restrictive due to the central memory requirement ($30MN$) for the ICCG method. The solution procedure used in DAISY is successive over-relaxation (SOR).[35]

The choice of the over relaxation parameter ω has an important influence on the number of iterations required for the SOR iterations to converge to a given accuracy. For simple problems it is possible to obtain an optimum ω with a minimum amount of effort. However, due to the complex nonlinear diffusion algorithm on a distorted mesh, the optimum relaxation parameter (ω) is obtained using a brute force approach: During a simulation ω is obtained internally in DAISY by monitoring the number of iterations required for convergence for a trial ω; trial ω's are then continually adjusted to maintain optimal results.

The proper boundary conditions for electron thermal diffusion is the zero gradient boundary condtion at a vacuum-fluid interface. To accommodate this no-flux condition, it is necessary to extend the computational grid when computing temperature gradients near a vacuum interface ("ghost cells"). The ghost cells are used only to enforce the boundary condition, and do not affect material zones in the problem. At slip surfaces we also use a zero temperature gradient condition.

3. Test problems

A. Linear Rayleigh–Taylor instability

Numerical simulations of Rayleigh–Taylor unstable flows in the absence of thermal conduction were performed to: (1) Compare the accuracy of DAISY hydrodynamics with analytic results[3,4] ;(2) Examine the sensitivity of these results to resolution (number of points per wavelength).

For $\alpha = 1$, a gas of uniform material density ρ_1, pressure P_0, and thickness Δx lies between two rigid parallel slip surfaces at $y = 0$ and $y = \lambda_y/2$. At the left vacuum boundary, the pressure is set to P_0, while that at the right boundary is set to zero. To compare DAISY results with linear theory, a perturbation using Eqs. (1) and (2) with $A/\lambda_y = 0.001$ is applied at the left vacuum-gas interface [x_m in Eq. (2) defines the interface location here]. To minimize finite thickness effects[3] we choose $k\Delta x \gg 1$. The equation of state for this test assumes a perfect gas with the ratio of specific heats set to ten to approximate an effectively imcompressible fluid.[36]

Shock transients are avoided by allowing the gas slab to expand freely to the right. The accelertion of the slab ($P_0 > 0$) is not initiated until the rarefaction reaches the left vacuum-gas boundary.

The linear growth rates are determined using: (1) The bubble center minus spike tip separation distance as a function of time; (2) The rms deviation of an i line. Both methods give essentially the same linear growth rates for the cases considered. The results of these calculations for a wide range of perturbation wavenumbers (k_y) and varying resolution are shown in Fig. 33, normalized by the analytic growth rate $\gamma_{\text{classical}}$. A resolution of sixteen zones per wavelength is adequate to determine the linear growth rate to better than 10% over the entire k_y range considered. However, increased resolution is needed to follow accurately the large amplitude (nonlinear) mode evolution.[11]

In the x direction, the number of zones is determined by the requirement that near the ablation surface resolution similar to that in the y direction be maintained throughout the simulation.

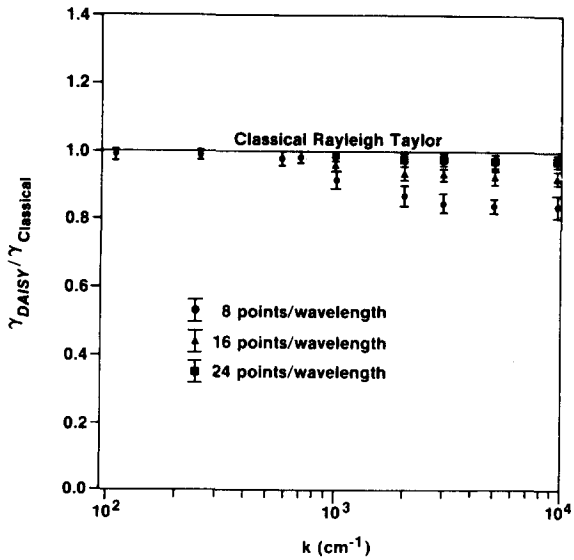

FIG. 33. Linear growth rates for the Rayleigh–Taylor instability calculated by DAISY for varying resolution compared to analytic results.

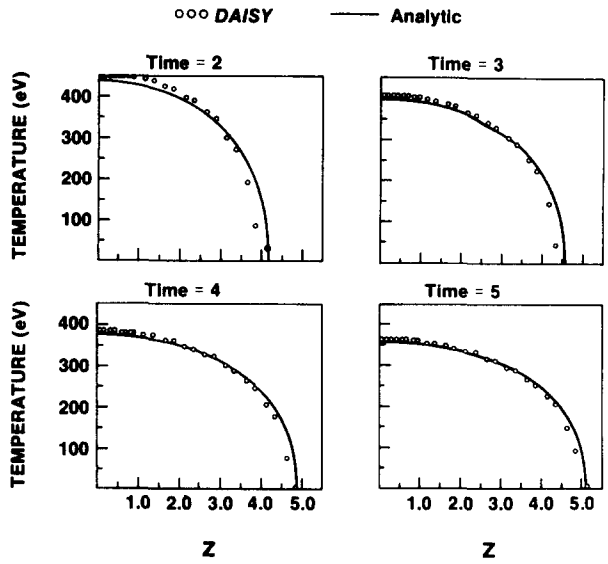

FIG. 34. Nonlinear thermal wave propagation test case. Open circles: DAISY results. Solid curves: Analytic results.

B. Nonlinear thermal diffusion

The differencing scheme used in DAISY for solving the thermal diffusion equation have been tested for a variety of problems, including both linear[37] ($\kappa = \text{const.}$) and nonlinear[38] ($\kappa = \kappa_0 T^n$) thermal wave propagation. The results for a thermal wave due to an instantaneous plane source propagating into cold material having a nonlinear conductivity with $n = 5/2$, for both $C_v, \rho = \text{const.}$ is shown in Fig. 34.

For this problem, $\Delta y/\Delta x$ for each zone is 10. This ratio is a challenging test case because only equilaterial triangles ($\Delta y/\Delta x = 1.16$) avoid contributions from all thirteen triangles (see Fig. 32). The ratio of the time step to the explicit time step required for the diffusion equation exceeded 200 for the results plotted in Fig. 34. The code results typically conserve energy to better than 0.1% in these examples, and the thermal front location is in agreement with the analytic result[38] to within one grid-point location.

APPENDIX B: DIPOLE SHEET EVOLUTION EQUATION FOR A FLUID LAYER

It is well-known that all potential fields may be constructed by means of surface distributions of sources or dipoles. The potential $\phi(P)$ due to a layer of sources distributed over some sufficiently smooth surface varies continuously as P passes through the surface at some point Q, but the normal derivative has a jump discontinuity at Q. The magnitude of the jump is directly related to the local strength of the source distribution. On the other hand, the value of a dipole-layer potential $\phi(P)$ has jump discontinuities, but the normal derivative varies continuously when P penetrates the surface along the normal at Q.

At the interface between two irrotational incompressible fluids, the normal velocity on either side must be continuous while the tangential velocity is discontinuous. Thus a representation of the potential ϕ of the flow by a dipole sheet satisfies the kinematic boundary condition at the interface.

Consider a distribution of dipoles μ on some curve C. If the arc length s is used to parametrize C, then the potential is given by

$$\phi(P) = -\int_C \mu(s)\frac{\partial}{\partial n_s}\log\left(\frac{1}{|r_s - r_p|}\right)ds, \tag{B1}$$

where r is the position vector, n_s is the outward normal, and C is traversed in the counterclockwise sense. It is useful to work in terms of complex coordinates. The kernel in (B1) becomes

$$\frac{\partial}{\partial n_s}\log\left(\frac{1}{|r_s - r_p|}\right) = \mathrm{Re}\left[\frac{\partial}{\partial n_s}\log\left(\frac{1}{|r_s - r_p|}\right)\right] = \mathrm{Im}\left(\frac{1}{z(P) - z(s)}\frac{dz}{ds}\right)$$

by the Cauchy–Riemann equations so that

$$\phi(P) = -\int_C \mu(s)\mathrm{Im}\left(\frac{1}{z(P) - z(s)}\frac{dz}{ds}\right)ds. \tag{B2}$$

In this paper the contour C represents the two periodic interfaces bounding the finite fluid layer. Rather than work in terms of arc length we introduce a Lagrangian variable e so that

$$z_1(e + 2\pi) = z_1(e) + 2\pi, \quad z_2(e + 2\pi) = z_2(e) + 2\pi.$$

We assume that the dipole distribution $\mu(e)$ is also periodic so that the integrals in (B2) can be written as sums:

$$\phi(P) = -\sum_{n=-\infty}^{\infty}\int_0^{2\pi}\mathrm{Im}\left(\frac{1}{z(P) - z_1(e') - 2\pi n}\frac{dz_1}{de'}\right)\mu_1(e')de' + \int_0^{2\pi}\mathrm{Im}\left(\frac{1}{z(P) - z_2(e') - 2\pi n}\frac{dz_2}{de'}\right)\mu_2(e')de'.$$

Using the formula

$$\pi\cot\pi z = \frac{1}{z} + \sum_{n=1}^{\infty}\left(\frac{1}{z - n} + \frac{1}{z + n}\right),$$

it follows that:

$$\phi(P) = -\frac{1}{2}\int_0^{2\pi}\mu_1(e')\,\mathrm{Im}\left[\cot\left(\frac{z(P) - z_1(e')}{2}\right)\right]\frac{dz_1}{de'}de' - \frac{1}{2}\int_0^{2\pi}\mu_2(e')\,\mathrm{Im}\left[\cot\left(\frac{z(P) - z_2(e')}{2}\right)\frac{dz_2}{de'}de'\right]. \tag{B3}$$

At each interface the principal value (PV) of the potential is the average of the limiting values of the potential obtained by approaching the interface from above the below:

$$\phi_1(e) = -\frac{1}{2}\mathrm{PV}\int_0^{2\pi}\mu_1(e')\,\mathrm{Im}\left[\cot\left(\frac{z_1(e) - z_1(e')}{2}\right)\frac{dz_1}{de'}\right]de' - \frac{1}{2}\int_0^{2\pi}\mu_2(e')\mathrm{Im}\left[\cot\left(\frac{z_1(e) - z_2(e')}{2}\right)\frac{dz_2}{de'}\right]de' \tag{B4}$$

$$\phi_2(e) = -\frac{1}{2}\int_0^{2\pi}\mu_1(e')\mathrm{Im}\left[\cot\left(\frac{z_2(e) - z_1(e')}{2}\right)\frac{dz_1}{de'}\right]de' - \frac{1}{2}\mathrm{PV}\int_0^{2\pi}\mu_2(e')\mathrm{Im}\left[\cot\left(\frac{z_2(e) - z_2(e')}{2}\right)\frac{dz_2}{de'}\right]de'.$$

Here ϕ_1 is the average potential at interface 1, while ϕ_2 is the average at interface 2. If ϕ_{1U}, ϕ_{1L} (ϕ_{2U}, ϕ_{2L}) represent the upper and lower limiting values at interface 1(2) then

$$\phi_{1U} - \phi_{1L} = 2\pi\mu_1(e), \quad \phi_{2U} - \phi_{2L} = 2\pi\mu_2(e). \tag{B5}$$

Using (B4) and (B5) the following coupled Fredholm integral equations for μ_1, μ_2 are obtained:

$$\mu_1(e) = -\frac{\phi_{1L}}{\pi} - \frac{1}{2\pi}\int_0^{2\pi}[\mu_1(e') - \mu_1(e)] \times \mathrm{Im}\left[\cot\left(\frac{z_1(e) - z_2(e')}{2}\right)\frac{dz_1}{de'}\right]de', - \frac{1}{2\pi}\int_0^{2\pi}\mu_2(e')\mathrm{Im}\left[\cot\left(\frac{z_1(e) - z_2(e')}{2}\right)\frac{dz_2}{de'}\right]de', \tag{B6}$$

$$\mu_2(e) = -\frac{\phi_{2L}}{\pi} - \frac{1}{2\pi}\int_0^{2\pi}\mu_1(e') \times \mathrm{Im}\left[\cot\left(\frac{z_2(e) - z_1(e')}{2}\right)\frac{dz_1}{de'}\right]de' - \frac{1}{2\pi}\int_0^{2\pi}[\mu_2(e') - \mu_2(e)] \times \mathrm{Im}\left[\cot\left(\frac{z_2(e) - z_2(e')}{2}\right)\frac{dz_2}{de'}\right]de', \tag{B7}$$

$$\mu_1(e) = +\frac{\phi_{1U}}{\pi} + \frac{1}{2\pi}\int_0^{2\pi}[\mu_1(e') - \mu_1(e)] \times \mathrm{Im}\left[\cot\left(\frac{z_1(e) - z_1(e')}{2}\right)\frac{dz_1}{de'}\right]de', + \frac{1}{2\pi}\int_0^{2\pi}\mu_2(e')\mathrm{Im}\left[\cot\left(\frac{z_1(e) - z_2(e')}{2}\right)\frac{dz_2}{de'}\right]de', \tag{B8}$$

$$\mu_2(e) = \frac{\phi_{2U}}{\pi} + \frac{1}{2\pi}\int_0^{2\pi}\mu_1(e') \times \mathrm{Im}\left[\cot\left(\frac{z_2(e) - z_1(e')}{2}\right)\frac{dz_1}{de'}\right]de' + \frac{1}{2\pi}\int_0^{2\pi}[\mu_2(e') - \mu_2(e)] \times \mathrm{Im}\left[\cot\left(\frac{z_2(e) - z_2(e')}{2}\right)\frac{dz_2}{de'}\right]de'. \tag{B9}$$

Here the kernel is regularized by using the identity

$$\mathrm{PV}\int\cot\left(\frac{z(e) - z(e')}{2}\right)\frac{dz}{de'}de' = 0. \tag{B10}$$

Given ϕ_{1L} or ϕ_{1U} and ϕ_{2L} or ϕ_{2U} it is possible to determine the dipole sheet strengths $\mu_1(e), \mu_2(e)$ from (B6–B9). The potential ϕ may then be determined at any point using (B3). If a free surface flow is being simulated it is also necessary to compute the normal derivative of the potential in order to advance the position of the interface forward in time. This is accomplished by computing the conjugate harmonic function to ϕ, namely, the stream function ψ. From (B3) it is clear that

$$\phi + i\psi = \frac{i}{2}\int_0^{2\pi}\mu_1(e')\cot\left(\frac{z(P) - z_1(e')}{2}\right)\frac{dz_1}{de'}de' + \frac{i}{2}\int_0^{2\pi}\mu_2(e')\cot\left(\frac{z(P) - z_2(e')}{2}\right)\frac{dz_2}{de'}de'. \tag{B11}$$

Therefore, at the interfaces,

$$\psi_1(e) = \frac{1}{2}\int_0^{2\pi}[\mu_1(e') - \mu_1(e)]\,\mathrm{Re}\left[\cot\left(\frac{z_1(e) - z_1(e')}{2}\right)\frac{dz_1}{de'}\right]de'$$

$$+\frac{1}{2}\int_0^{2\pi}\mu_2(e')\,\mathrm{Re}\left[\cot\left(\frac{z_1(e)-z_2(e')}{2}\right)\frac{dz_2}{de'}\right]de',$$

and

$$\psi_2(e)=\frac{1}{2}\int_0^{2\pi}\mu_1(e')\mathrm{Re}\left[\cot\left(\frac{z_2(e)-z_1(e')}{2}\right)\frac{dz_1}{de'}\right]de'$$
$$+\frac{1}{2}\int_0^{2\pi}[\mu_2(e')-\mu_2(e)]$$
$$\times\mathrm{Re}\left[\cot\left(\frac{z_2(e)-z_2(e')}{2}\right)\frac{dz_2}{de'}\right]de'. \tag{B12}$$

The Cauchy–Riemann equations imply

$$\frac{\partial\phi}{\partial n_s}=\frac{\partial\psi}{\partial s}=\frac{\partial\psi/\partial e}{\partial s/\partial e}.$$

The equations (B6–B9) for $\mu_1(e)$ and $\mu_2(e)$ may be solved numerically by evaluating the equation at N discrete points and inverting the resulting matrix. This procedure becomes expensive as N becomes large. An alternative is to iterate for the solution. In particular for (B6–B7) the Neumann series iterates are:

$$\mu_{1,n+1}(e)=-\frac{\phi_{1L}(e)}{\pi}-\frac{1}{2\pi}\int_0^{2\pi}[\mu_{1,n}(e')-\mu_{1,n}(e)]$$
$$\times\mathrm{Im}\left[\cot\left(\frac{z_1(e)-z_1(e')}{2}\right)\frac{dz_1}{de'}\right]de'$$
$$-\frac{1}{2\pi}\int_0^{2\pi}\mu_{2,n}(e')$$
$$\times\mathrm{Im}\left[\cot\left(\frac{z_1(e)-z_2(e')}{2}\right)\frac{dz_2}{de'}\right]de',$$
$$\mu_{2,n+1}(e)=-\frac{\phi_{2L}}{\pi}-\frac{1}{2\pi}\int_0^{2\pi}\mu_{1,n}(e')$$
$$\times\mathrm{Im}\left[\cot\left(\frac{z_2(e)-z_1(e')}{2}\right)\frac{dz_1}{de}\right]de'$$
$$-\frac{1}{2\pi}\int_0^{2\pi}[\mu_{2,n}(e')-\mu_{2,n}(e)]$$
$$\times\mathrm{Im}\left[\cot\left(\frac{z_2(e)-z_2(e')}{2}\right)\frac{dz_2}{de'}\right]de'. \tag{B13}$$

A study of the eigenvalues of the kernel in (B5) reveals that the sequence $\mu_{1,n}(e)$, $\mu_{2,n}(e)$ given by (B13) will always converge for any boundary curve that is twice differentiable. However, the convergence of the discrete version of (B13) used in the numerical integration depends strongly on the distribution of markers over the boundary. The rate of convergence is dominated by the largest eigenvalue. As the boundary becomes increasingly distorted away from two parallel flat interfaces, the largest eigenvalue approaches 1. However, in practice only a modest number of interations is required to compute $\mu_1(e)$ and $\mu_2(e)$ to an accuracy of 1 part in 10^5 for geometries with amplitude-to-wavelength ratios as large as 2 to 1.

Finally, we give the evolution equation for the dipole sheet strength $\mu_1(e)$:

$$\frac{D\mu_1}{Dt}=-\frac{1}{\pi}\alpha\left\{\frac{D\phi_1}{Dt}-\frac{1}{2}\left[\left(\frac{\partial\phi_1}{\partial s}\right)^2+\left(\frac{\partial\phi_1}{\partial n_s}\right)^2\right]\right.$$
$$\left.+\frac{1}{2}\pi^2\left(\frac{\partial\mu_1}{\partial s}\right)^2+gy\right\}, \tag{B14}$$

where α is the Atwood ratio, $\alpha\equiv(\rho_{1U}-\rho_{1L})/(\rho_{1U}+\rho_{1L})$ and $\rho_{1L,U}$ refer to the fluid densities below and above interface 1. A similar equation holds for $D\mu_2/Dt$. The time derivative in (B14) represents Lagrangian motion with respect to the average velocities across the interface. Equation (B14) may be modified so that the motion of the interface markers is determined by a weighted average of the upper and lower fluid velocities.[12] The resulting evolution equation is:

$$\frac{D\mu_1}{Dt}=-\frac{\alpha}{\pi}\left\{\frac{D\phi_1}{Dt}-\frac{1}{2}\left[\left(\frac{\partial\phi_1}{\partial s}\right)^2+\left(\frac{\partial\phi_1}{\partial n_s}\right)^2\right]\right.$$
$$+gy+\tfrac{1}{2}\pi^2\left(\frac{\partial\mu_1}{\partial s}\right)^2$$
$$\left.-\frac{\beta}{2}\left(\frac{\partial\phi_1}{\partial s}\right)\left(\frac{\partial\mu_1}{\partial s}\right)\right\}+\frac{\beta}{2}\left(\frac{\partial\mu_1}{\partial s}\right)^2. \tag{B15}$$

Again, a similar equation obtains for $D\mu_2/Dt$. For $\beta=0$, the evolution equation refers to the average evolution of the sheet considered, while for $\beta=+2\pi(-2\pi)$ the sheet strength considered becomes that of the upper (lower) fluid of each interface. Note that (B15) also represents a coupled system of Fredholm integral equations of the second kind. These are more useful in a time dependent simulation as the desired quantities are the time derivations of μ_1,μ_2. Further details are given in Ref. 12. Note that the dipole sheet density μ of Ref. 12 is -2π times the μ used here.

[1] G. Fraley, W. Gula, D. Henderson, R. McCrory, R. Malone, R. Mason, and R. Morse, in *Plasma Physics and Controlled Nuclear Fusion Research, Tokyo, Japan, 1974* (International Atomic Energy Agency, Vienna, Austria, 1974), p. 543.
[2] R. J. Mason, Nucl. Fusion **15**, 1031 (1975).
[3] G. Taylor, Proc. Roy. Soc. A **201**, 192 (1950).
[4] S. Chandrasekhar, *Hydrodynamic and Hydromagnetic Stability* (Oxford University Press, Oxford, England, 1961), Chap. 10.
[5] R. L. McCrory, L. Montierth, R. L. Morse, and C. P. Verdon, in *Laser Interaction and Related Plasma Phenomena* (Plenum, New York, 1981), Vol. 5, pp. 713–742.
[6] R. L. McCrory, R. L. Morse, and K. A. Taggart, Nucl. Sci. Eng. **64**, 163 (1977).
[7] L. Montierth, F. L. Cochran, and R. L. Morse, Bull, Am. Phys. Soc. **24**, 945 (1979).
[8] R. L. McCrory, L. Montierth, R. L. Morse, and C. P. Verdon, Phys. Rev. Lett. **46**, 336 (1981).
[9] E. G. Gamalii, V. B. Rozanov, A. A. Samarskii, V. F. Tishkin, N. N. Tyurina, and A. P. Favorskii, Zh. Eksp. Teor. Fiz. **79**, 459 (1980) [Sov. Phys. JETP **52**, 230 (1980)].
[10] S. J. Gitomer, R. L. Morse, and B. S. Newberger, Phys. Fluids **12**, 234 (1977).
[11] G. R. Baker, D. I. Meiron, and S. A. Orszag, Phys. Fluids **23**, 1485 (1980). A term involving dS/dt, inadvertently omitted, should appear in Eq. (2) of this reference.
[12] G. R. Baker, D. I. Meiron, and S. A. Orszag, J. Fluid Mech. (in press).
[13] L. Spitzer, *Physics of Fully Ionized Gases* (Interscience, New York, 1961).
[14] K. Estabrook and W. L. Kruer, Phys. Rev. Lett. **40**, 42 (1978).
[15] C. E. Max, C. F. McKee, and W. C. Mead, Phys. Fluids **23**, 1620 (1980).
[16] F. H. Harlow and J. E. Welch, Phys. Fluids **9**, 842 (1966).
[17] B. J. Daly, Phys. Fluids **10**, 297 (1967).
[18] J. R. Freeman, M. J. Clauser, and S. L. Thompson, Nucl. Fusion **17**, 223 (1977).
[19] J. D. Lindl and W. C. Mead, Phys. Rev. Lett. **34**, 1273 (1975).
[20] G. Birkhoff, Los Alamos Scientific Laboratory Report No. LA-1927 (1956) and LA-1862 (Appendix F by E. Fermi) (1955).
[21] R. L. McCrory and R. L. Morse, Phys. Fluids **19**, 175 (1976).
[22] Yu. V. Afanas'ev, N. G. Basov, P. P. Volosevich, E. G. Gamalii, S. P. Kurdyumov, O. N. Krokhin, E. I. Levanov, V. B. Rozanov, A. A. Samarskii, and A. N. Tikhonov, Pis'ma Zh. Eksp. Teor. Fiz. **21**, 150 (1975)

[JETP Lett. **21**, 68 (1975)], Yu. V. Afanas'ev, N. G. Basov, E. G. Gamalii, N. O. Krokhin, and V. B. Rozanov, Pis'ma Zh. Eksp. Teor. Fiz. **23**, 617 (1976) [JETP Lett. **23**, 566 (1976)].
[23]D. B. Henderson and R. L. Morse, Phys. Rev. Lett. **32**, 355 (1973); see also J. N. Shiau, E. B. Goldman, and C. I. Weng, Phys. Rev. Lett. **32**,352 (1973).
[24]D. B. Henderson, R. L. McCrory, and R. L. Morse, Phys. Rev. Lett. **33**, 205 (1974).
[25]S. E. Bodner, Phys. Rev. Lett. **33**, 761 (1974).
[26]G. N. White, Los Alamos Scientific Laboratory Report No. LA-5575-MS (1974).
[27]H. G. Horak, E. M. Jones, J. W. Kodis, and M. T. Stanford,II, J. Comput. Phys. **26**, 277 (1978).
[28]J. U. Brackbill and J. S. Saltzman, Los Alamos Scientific Laboratory Report No. LA-UR-81-405 (1981).
[29]J. von Neumann and R. D. Richtmyer, J. Appl. Phys. **21**, 232 (1950).
[30]W. D. Schulz, in *Methods in Computational Physics*, edited by B. Alder, S. Fernback,and M.Rotenberg (Academic, New York, 1964), Vol. 3, pp. 1–45.
[31]G. T. Richards, Lawerence Livermore Laboratory Report No. UCRL-14244 (1965).
[32]J. W. White, J. Comput. Phys. **11**, 573 (1973).
[33]P. L. Browne and K. B. Wallick, Los Alamos Scientific Laboratory Report No. LA-4740-MS. (1971).
[34]D. S. Kershaw, J. Comput. Phys. **26**, 43 (1978).
[35]W. S. Dorn and D. D. McCracken, *Numerical Methods with Fortran* IV *Case Studies* (Wiley, New York, 1972), Chap. 4.
[36]W. C. Mead and J. D. Lindl, Lawerence Livermore Laboratory Report No. UCRL-77057 (1975).
[37]H. S. Carslaw and J. D. Jaeger, *Conduction of Heat in Solids* (Clarendon, Oxford, 1959).
[38]Ya. B. Zel'dovich and Yu. P. Raizer, *Physics of Shock Waves and High-Temperature Hydrodynamic Phenomena* (Academic, New York, 1967), Vol II, Chap. 10.